

How adaptive immunity constrains composition and fate of large bacterial populations

Madeleine Bonsma-Fisher¹, Dominique Soutière¹, and Sidhartha Goyal^{1,2}

¹Department of Physics, University of Toronto, 60 St George St, Toronto, ON M5S 1A7

²Institute of Biomaterials & Biomedical Engineering, University of Toronto, 164 College Street, Toronto, ON M5S 3G9

Abstract

Features of the CRISPR-Cas system, in which bacteria integrate small segments of phage genome (spacers) into their DNA to neutralize future attack, suggest its effect is not limited to individual bacteria but may control the fate and structure of whole populations. Emphasizing the population-level impact of the CRISPR-Cas system, recent experiments show that some bacteria regulate CRISPR-associated genes via the quorum sensing (QS) pathway. Here we present a model that shows that from the highly stochastic dynamics of individual spacers under QS control emerges a rank-abundance distribution of spacers that is time-invariant, a surprising prediction that we test with dynamic spacer-tracking data [1]. This distribution depends on the state of the competing phage-bacteria population, which due to QS-based regulation may coexist in multiple stable states that vary significantly in their phage-to-bacterium ratio, an ecological measure of such systems.

1 Introduction

All living things from bacteria to humans must contend with pathogenic viruses that invade and infect them. When under attack, many organisms, including individual bacteria, first initiate a largely non-specific immune response that heightens surveillance of foreign material [2, 3]. Such a non-specific response may fall short to resist infections by more potent viruses, and may require an adaptive system which flexibly and dynamically responds to specific threats by learning from past encounters to better resist future infections. Previously thought to be a vertebrate trait, such an adaptive immune system has recently been discovered in bacteria and archaea. While having such a system may significantly improve a bacterium's odds against predatory viruses (called phages), there may be a direct physiological cost of maintaining and utilizing such a system [4, 5]. How this trade-off may constrain the fate of co-existing phage-bacteria populations remains unaddressed.

Machinery for adaptive immunity in bacteria (called CRISPR-Cas), when activated, allows them to acquire unique genetic elements (called spacers) from prior phage encounters to specifically target and evade recurrent attacks. The spacers are 10s of nucleotides long, and at each encounter may be acquired from any of the 100s of possible locations on the infecting phage genome (called protospacers). Since individual spacers are distinguishable and because they are integrated in the genome, the result is a lineage of cells that can be identified by its spacer(s). The fate of an individual lineage, however, is subject to large fluctuations as lineages intertwine with stochastic dynamics of individual bacteria in a large rapidly evolving population. Experiments show that the abundance of individual spacers in a bacterial population under phage attack is indeed highly dynamic and varies over several orders of magnitude from one spacer to the next [6, 7, 8, 1, 9]. This leads to a natural question: What controls

spacer diversity and abundance; in other words, how does recurrent phage attack alter the structure and composition of interacting spacer-marked lineages in a bacterial population?

Recently, similar questions about diversity in the adaptive immune system have gained traction in the context of vertebrates. Unlike bacteria that acquire information directly from the phage genome, vertebrates generate and maintain a large population of specialized immune cells that, as a group, contain an extremely diverse set of binding sites that individually recognize different viruses. Like spacer abundance, the abundance of individual binding sites is highly variable and has been shown to be distributed in a particular way across several vertebrate species [10, 11, 12]. This observation has led to the suggestion that a broad abundance distribution of binding sites may strike a balance between generating a rapid response against likely invaders with capturing new invaders [12]. Although this is hard to test in vertebrates, laboratory experiments that alter bacterial population composition synthetically show that bacteria are more successful at fending off phages as their population-level spacer diversity increases [13]. How the dynamics of individual bacterial lineages shape spacer diversity and how diversity in spacer sequences or *types* relates to diversity in spacer *abundances* remains unanswered.

Previous population-level models of bacteria-phage interactions with CRISPR-Cas have focused mainly on the parameter regimes in which phage and bacteria coexist and the nature and stability of coexistence [14, 15, 16, 17, 18, 19, 20, 21]. More complicated population effects have been explored in the context of innate immunity [22, 23], biofilms [24], variable or time-varying parameters [25], and spatially structured populations [14, 26, 27], but not in the context of regulation of CRISPR-Cas expression which could have important ecological impacts on the population. Recent experiments have shown that bacterial populations exert top-down control on the CRISPR system: two species of bacteria have been observed to regulate their CRISPR-Cas systems in response to cell density [28, 29]. Interestingly, this control acts via the quorum sensing pathway, a pathway which also controls population-level responses such as virulence. This suggests a different paradigm where the effects of CRISPR-Cas need to be considered at the collective population level, rather than at the level of individual cells. For example, Høyland-Kroghsbo *et al.* [28] have suggested that CRISPR-Cas regulation could drastically limit the effectiveness of phage therapy in dense bacterial populations such as biofilms. Modelling efforts addressing CRISPR-Cas regulation have focused on the relevant gene circuits and production of transcribed spacers called CRISPR RNAs (crRNAs), not on the population-level effects of regulation [30, 31, 32].

In the presence of CRISPR-Cas it has proved challenging to reconcile the observed high diversity of spacers, both in laboratory experiments and in natural populations, with the observed long-term coexistence of bacteria and phages. Several previous models have addressed the role and dynamics of observed diversity of spacer types [33, 34, 35, 27, 36, 37, 38, 20] in a qualitative way: (1) how system parameters such as phage adsorption rate [20], spacer acquisition rate [35, 20], and phage mutation and recombination [36] affect spacer diversity, (2) how increasing diversity promotes population stability [35, 37], and (3) have reproduced the observed asymmetry in diversity along the locus in natural populations [33, 34, 36] by modelling biased acquisition at the leader end of the CRISPR locus. Most recently, Bradde *et al.* [38] show a connection between spacer acquisition rates and spacer effectiveness to spacer diversity. To make a direct connection with data, we analyzed sequencing data from Paez-Espino *et al.* [1], where they performed a co-evolution experiment with phage and bacteria and tracked spacer dynamics. Our analysis shows that despite rapid turnover of individual spacer types the spacer abundance distribution quickly stabilizes, which is a new and striking observation that previous models have not addressed.

We build a model that addresses the two aforementioned fundamental and unaddressed aspects of the CRISPR-Cas system: (1) our model shows how stable spacer abundance distributions may arise despite rapid turnover of individual spacer types, and (2) our model shows that density-dependent regulation of CRISPR-Cas admits a new bistable state at the population level where the phage-bacterial population can be stable with two different configurations under the same external conditions. We further argue how having the knowledge of spacer diversity along with bistable states may shed

light on the fate of natural microbial populations.

2 Model

Adaptive immunity in bacteria is controlled by a set of Cas proteins, which in a nutshell accomplish two different tasks. (1) When an invading phage inserts its genome into a bacterial cell but is not successful in killing the bacterium, Cas proteins take a small piece of phage genome and insert it into the bacterial genome at a specific site called the CRISPR locus. (2) During a subsequent phage attack, the bacterium can use the information stored in the CRISPR locus to recognize the invading phage and neutralize it. Multiple spacers can be stored at a CRISPR locus, providing a genetic record of immunization that is inherited during DNA replication. The immunization record in principle can be read via next generation sequencing and provides a rich presence/absence observable: s_{ijk} labelling each unique spacer with a type i , its locus position j , and its host bacterium label k , see Fig. 1A.

$$s_{ijk}(t) = \begin{cases} 1 & \text{if spacer type } i \text{ is at position } j \text{ in bacterium } k \\ 0 & \text{otherwise} \end{cases} \quad (1)$$

We model the abundance of the i^{th} spacer, $n_B^i(t)$, which is obtained by summing over all bacteria and locus positions, *i.e.* $n_B^i(t) = \sum_{j,k} s_{ijk}(t)$. An important simplifying assumption of our model is that each locus has at most one spacer, *i.e.* $j = 1$; this assumption is borne out of analysis of a laboratory experiment that shows that spacer dynamics stabilize rapidly within tens of generations with each bacterium predominantly having one new spacer (see Appendix A.2 for details of data analysis) [1]. Additionally, a model that allowed more than one spacer also found that only the most recently acquired spacers dominate the dynamics [35]. With this assumption, the abundance of individual spacer types can be mapped to the number of bacteria with a particular spacer, which means that n_B^i in our model maps to the number of bacteria with spacer type i . In addition, we assume each spacer to have equal effectiveness; this is both a simplifying assumption and also acknowledges our lack of experimental knowledge about differences among spacers and their effectiveness.

To capture the inherent stochastic nature of spacer dynamics, we model the probability distribution $P(n_B^0, \{n_B^i\}, n_V, C, t)$, which is the probability at time t of observing n_B^0 bacteria without spacers, $\{n_B^i\}$ bacteria with spacer type i , n_V phages, and a nutrient concentration of C . Interactions included in the model are illustrated in Figure 1B and described in detail in Appendix B. This construction highlights another important simplifying assumption which is also valid for short timescales: lack of phage diversity, *i.e.* all phages are assumed to be identical. Further work will address the phenomena of phage escape via mutations and recombination which have been experimentally observed [39, 9]. In addition, we model the phage-bacteria population in a flow cell or *chemostat*, a well-stirred vessel in which nutrients flow in at a constant rate and concentration and the mixture flows out with the same rate. A chemostat is not only comparable to periodic dilution experiments in the laboratory, it is also a reasonable approximation of real-world microbial populations from a gutter to a gut. In many of these natural environments, nutrients and waste flow in and out — the environment is not static like a petri dish. Additionally, the chemostat flow rate F is an experimental “knob” that can be used to tune a population-level bifurcation we describe later.

Our stochastic model has a corresponding mean-field or population-level description for average values of the different random variables, each represented by the same symbol as their corresponding random variable. At the mean-field level, all the spacer-containing bacteria can be pooled into a single variable $n_B^s = \sum_i n_B^i$, and the number of bacteria without spacers is n_B^0 . The mean-field equations are given in Equations. 2 to 5. Parameter descriptions and default values are shown in Table 1. We assume that the bacterial growth rate is linear with the concentration of nutrients C (equations 3 and 4). In reality the growth saturates, *i.e.* $gC/(C + k)$, where k is the nutrient concentration at which bacteria reach half-maximum growth rate. Introducing this growth rate into the model does not qualitatively change our results (see Appendix C.2).

Table 1: Model parameters

Parameter	Description	Value
$\frac{1}{gC_0}$	Bacterial doubling time	41.7 min
C_0	Inflow nutrient concentration in units of bacterial cell density	
α	Phage adsorption rate	$2 \times 10^{-10} \text{ min}^{-1}$
B	Phage burst size	170
F	Chemostat flow rate	
p_V	Probability of phage success for bacteria without spacers	
e	Spacer effectiveness	
r	Rate of spacer loss	
η	Probability of spacer acquisition	

Parameter values are as above unless otherwise indicated. Representative values estimated for *Streptococcus thermophilus* bacteria in lab conditions.

$$\frac{dn_V}{dt} = \underbrace{-\alpha n_V (n_B^s + n_B^0)}_{\text{phage adsorption}} + \underbrace{\alpha B p_V n_V (n_B^s (1-e) + n_B^0)}_{\text{phage burst}} - \underbrace{F n_V}_{\text{flow out}} \quad (2)$$

$$\frac{dn_B^0}{dt} = \underbrace{g C n_B^0}_{\text{growth}} - \underbrace{\alpha p_V n_V n_B^0}_{\text{bacterial lysis}} - \underbrace{\alpha (1-p_V) \eta n_V n_B^0}_{\text{spacer acquisition}} + \underbrace{r n_B^s}_{\text{spacer loss}} - \underbrace{F n_B^0}_{\text{flow out}} \quad (3)$$

$$\frac{dn_B^s}{dt} = \underbrace{g C n_B^s}_{\text{growth}} - \underbrace{\alpha p_V (1-e) n_V n_B^s}_{\text{bacterial lysis}} + \underbrace{\alpha (1-p_V) \eta n_V n_B^0}_{\text{spacer acquisition}} - \underbrace{r n_B^s}_{\text{spacer loss}} - \underbrace{F n_B^s}_{\text{flow out}} \quad (4)$$

$$\frac{dC}{dt} = \underbrace{F C_0}_{\text{flow in}} - \underbrace{g C (n_B^s + n_B^0)}_{\text{bacterial growth}} - \underbrace{F C}_{\text{flow out}} \quad (5)$$

3 Results

3.1 Mean-field steady-states

For phages to invade a bacterial population that is stable in a chemostat, their probability of successfully infecting bacteria without the benefits of adaptive immunity, p_V , needs to be above a certain minimum value given by $p_V^0 = \frac{1}{B} \left(\frac{gf}{(1-f)\alpha} + 1 \right)$, where $f = F/(gC_0)$. For $\frac{gf}{(1-f)\alpha} \ll 1$ (satisfied at the parameters we use for low flow rates), p_V^0 is approximately $1/B$: phages must succeed approximately every $1/B$ interactions in order to persist in the population. p_V^0 is surprisingly small for realistic values of the burst size B ; for example if $B = 100$, then $p_V^0 \approx 0.01$. As p_V rises above the threshold value, the steady-state phage population, n_V , first rises while the bacterial population decreases as they get killed by phages. Interestingly, the steady-state bacterial population keeps decreasing with increasing p_V , but the phage population exhibits a non-monotonic behaviour with a maximum population size at an intermediate value of $p_V^* = p_V^0 + \sqrt{\frac{p_V^0}{f} (p_V^0 - \frac{1}{B})}$. This steady-state behavior is qualitatively the same for bacteria with adaptive immunity ($e > 0$) as for bacteria without adaptive immunity ($e = 0$). Quantitatively, however, bacteria always fare better in the presence of adaptive immunity (Figure 2A). One surprising observation is that the minimum success probability required for phages to invade a bacterial culture is independent of adaptive immunity.

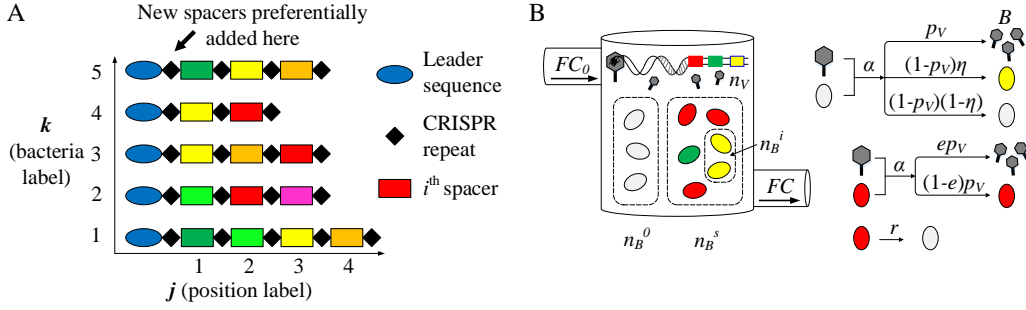


Figure 1: Overview of model. (A) CRISPR locus: Small (~ 30 nt) samples of invasive phage DNA called spacers (coloured rectangles) are incorporated into the CRISPR genetic locus. Spacers are separated by short (~ 30 nt) sequences called repeats (black diamonds). Multiple spacers can be stored at a CRISPR locus, resulting in a genetic record of immunization [40]. In the data shown in Figure 3A-C, we identify spacers with a type i , a locus position j , a bacterium k . (B) Bacteria and phages interact in a chemostat (flow cell) with a constant inflow and outflow rate F . Nutrients flow into the chemostat at a fixed concentration C_0 . Phages are assumed to be identical with a large, fixed number of possible protospacers. Phages adsorb to bacteria with rate α and successfully infect and kill naive bacteria with probability p_V . Each bacterium can acquire a single spacer. Spacers are tracked in the population as the number of bacteria containing a spacer of type i , n_B^i . If a naive bacterium survives an infection, it can acquire a spacer with probability η . All spacers are assumed to be equally effective: the probability of phage success in an infection is reduced by e if a bacterium has a spacer. Bacteria with spacers revert to naive bacteria by losing a spacer with rate r .

Much like increasing p_V , an increasing spacer effectiveness e causes the total number of bacteria at steady-state to increase monotonically (Figure 2B), since a bacterium with a spacer is less likely to be killed by phages as e increases. However, even for $e > 0$, not all bacterial cells in a population have a spacer, and the steady state fraction of the bacterial population with spacers, ν , is governed by a balance of spacer acquisition, η spacer loss, r , and the effect of e on the bacterial population. As a result, the steady-state level of bacteria can increase by either increased spacer acquisition or improved spacer effectiveness; contours in Figure 2B show the tradeoff between η and e that maintains bacterial population size.

In contrast to total bacterial population, the spacer-containing fraction ν first increases as e increases but reaches a maximum at an intermediate value of e (Figure 2C). This can be understood as ν qualitatively tracking the phage population size, which shows a peak at intermediate spacer effectiveness (see Appendix C.3 Figure 16). Qualitatively, this behavior is similar to the total phage population having a non-monotonic behaviour with increasing p_V .

3.2 Spacer abundance distributions

Even at steady-state with stable populations of phage and bacteria, the individual spacer abundances in the bacterial population are highly dynamic and vary significantly over time. This has been seen most directly in laboratory experiments [1, 9] but has also been observed in natural samples such as a hypersaline lake [41], human saliva [42], and acid mine drainage [6, 34]. This continual spacer turnover is influenced by bacterial reproduction and death, spacer acquisition, and spacer loss, all of which have been observed in natural and laboratory populations.

In our stochastic model, we keep track of individual spacer acquisition and loss events. Not surprisingly, we find that spacer abundances fluctuate over time (see Figure 3D and 3E). However, we also find that the spacer rank-abundance distribution reaches a stationary state, as shown in Figure

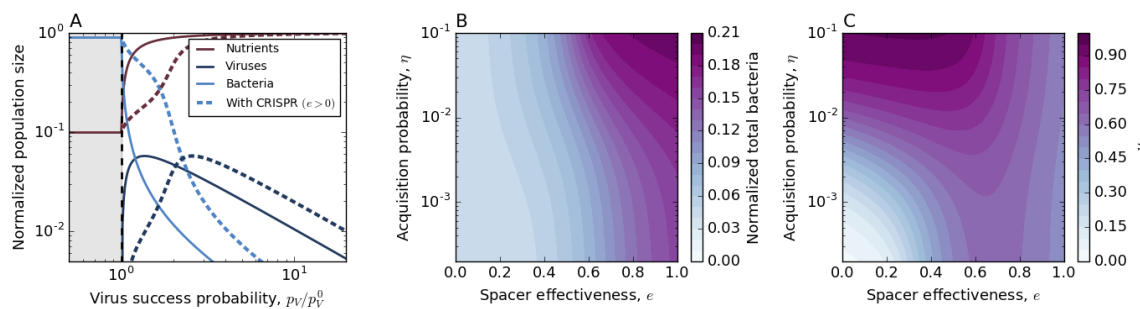


Figure 2: (A) Bacteria, phage, and nutrient populations at steady state as a function of the probability of phage success (p_V) for a model without CRISPR ($e = 0$, solid lines) and for a model where bacteria have CRISPR systems and are able to acquire spacers ($e = 0.5$, dashed lines). As the probability of phage success (p_V) increases, bacteria decrease in number. Below $p_V^0 = \frac{1}{B} \left(\frac{gf}{(1-f)\alpha} + 1 \right)$ where $f = F/(gC_0)$, phages cannot persist. Phages increase with increasing p_V and then decrease at high p_V because the bacterial population is too small to support more phages. (B) Normalized total bacteria as a function of spacer acquisition probability (η) and spacer effectiveness (equal for all spacers). (C) Fraction of bacteria with CRISPR spacers (ν) as a function of η and e .

3F. Not only does the spacer distribution in our simple model reach a stationary state while individual spacers turn over rapidly, it also shows 1000-fold variation in spacer abundances. The exact shape of the distribution depends on various parameters (see Appendix B.5) and may also change as various restrictive assumptions in the model are relaxed.

To test predictions with data, we analyzed experimental data reported by Paez-Espino et al. [1] from a bacterial population under constant phage attack. We summarized their raw sequencing data into the presence absence tensor s_{ijk} as shown in Fig. 1A and Eq. 1, and we tracked dynamics of individual spacers $n_B^i(t) = \sum_{j,k} s_{ijk}(t)$. Our analysis showed that abundance of individual spacer types fluctuated throughout the 15 days (~ 80 generations) of the experiment (3A), with more than 40% of spacers turning over within a few generations (Figure 3B). In contrast, we find that the spacer rank-abundance distribution reaches a stationary state, as shown in Figure 3C. Notably, the abundance distribution is broad with some spacers having a roughly 1000-fold higher abundance than others. However, in contrast to the intuition that highly abundant spacers may be more effective, these high-abundance spacers also experience continual turnover (see Appendix C.3.3 Figure 18 for details).

In general our analysis highlights that individual spacer identity and abundance may not themselves be important but collectively may provide a time-invariant observable in the form of steady-state spacer abundance distributions. And somewhat counterintuitively, spacers need not be functionally different in their effectiveness or acquisition probability to get large variability in spacer abundances.

3.3 Regulation of *cas* expression

Merely having an effective spacer, however, is not enough: to effectively neutralize phage, bacteria need to express *cas* genes when under attack. Experimental work has shown that bacteria can regulate their CRISPR-Cas systems in response to cell density, controlled under the quorum sensing pathway [28, 29]. A cell increases its expression of Cas proteins at high cell density in response to a high concentration of quorum sensing molecules and down-regulates its expression of Cas proteins at low cell density. To understand the role of cell density-dependent regulation of the CRISPR-Cas system, we made spacer effectiveness e to be a *constitutive* function of cell-density, represented as a Hill function characterized by three numbers: minimum effectiveness, e_{min} , maximum effectiveness, e_{max} , and typical population

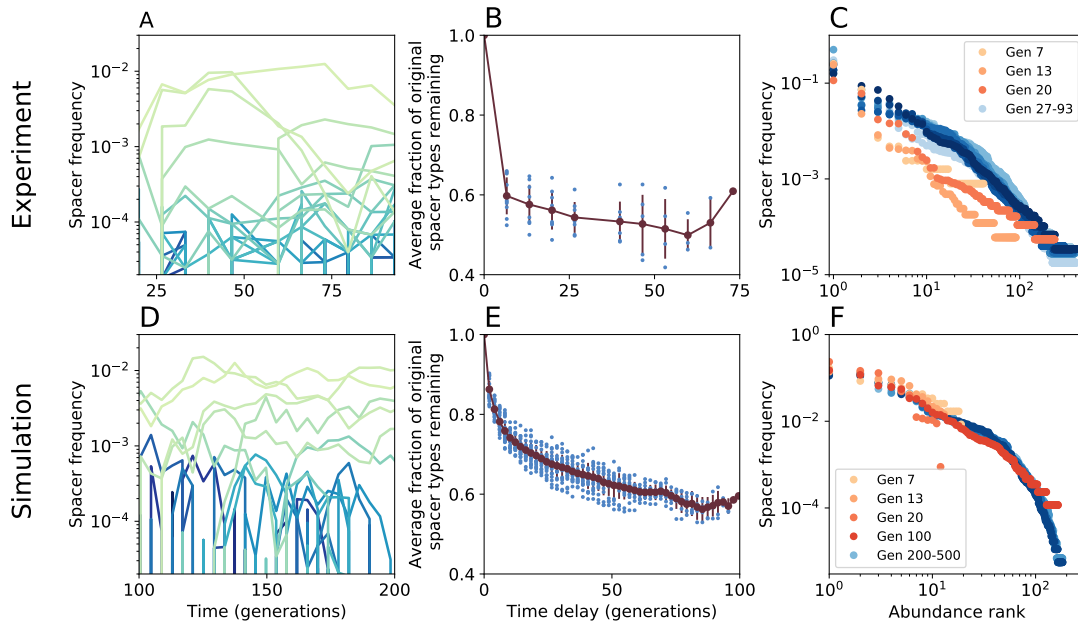


Figure 3: Comparison of spacer distributions between simulations (D-F) and experimental data from [1] (A-C). (A) and (D) Subset of spacer type trajectories for experimental data (A) and simulated data with $\eta = 10^{-5}$ and $e = 0.387$ (D). Qualitative simulation results are insensitive to the choice of e and η . Individual spacer abundances fluctuate throughout the experiment and simulation. (B) Fraction of spacer types with a non-zero abundance that continue to have a non-zero abundance at subsequent time points (blue points), averaged over all starting points (red line) at steady-state from generation 26 (Day 4 of the experiment) onwards. Error bars are the standard deviation of all fractions with the same time delay. (E) Same as (B) but for simulated data. (C) The rank-abundance distribution of spacer clone sizes reaches a steady state in the experiment after about 20 generations (Day 3 of the experiment). (F) The distribution of spacer clone sizes reaches a steady state in the simulation after about 100 generations. Plotted is the same quantity as in (C). Even after the distribution of clone sizes has reached steady state, individual spacer types experience continual turnover.

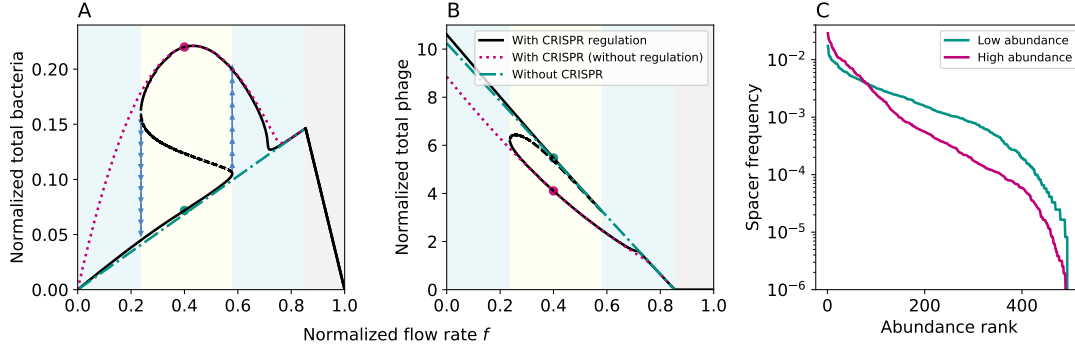


Figure 4: Bacterial upregulation of *cas* gene expression at high density can induce bistability (yellow shaded area) as a function of the flow rate, a parameter that is easy to tune experimentally. The blue shaded region is monostable, and in the grey shaded region phages cannot persist. (A) The bacterial population size (solid black lines) exhibits hysteresis (blue arrows) between a low-expression, low-density state and a high-expression, high-density state. (B) Phages also exhibit bistability, reaching a lower steady-state population size when *cas* expression is high and a higher population size when expression is low. (C) The shape of the spacer rank-abundance distribution depends on the ecological state of the population. Plotted are two rank-abundance distributions from simulations of the high and low expression states respectively, with the population sizes for each distribution indicated by the coloured dots in (A) and (B). Bacteria and phage counts are scaled by the initial nutrient concentration C_0 .

size where the behaviour changes from low to high effectiveness (see Appendix E). Regulation of *cas* genes may also alter other parameters of the model such as acquisition, spacer loss, and growth rates, but we show in Appendix E.3 that adding regulation to other possible parameters independent of effectiveness has little effect, and that in conjunction with density-dependent effectiveness they do not change the qualitative features we describe below.

Notably, the dependence of spacer effectiveness on population size changes both the number and value of the steady-state fixed points. We find that the whole bacteria-phage-nutrient system undergoes a saddle-node bifurcation and is bistable for a range of parameters. There are various parameters that can be used as the bifurcation parameter, but one that can be easily controlled in experimental systems and perhaps plays a role in natural systems is the flow rate f , which can also be thought of as the inverse of nutrient availability. Figure 4 shows how bacterial and phage abundance varies as flow rate is changed in the presence of density-dependent regulation of the CRISPR-Cas system. At the two extremes, for low flow rate the system behaves with no adaptive immunity and bacterial (and phage) population size is low, while at high flow rate adaptive immunity kicks in and bacteria can maintain a higher population size. The phage population remains low at high flow rate both because bacteria are more resistant and because phages are removed from the system at a higher rate. At very high flow rate, phages go extinct and the bacterial population starts decreasing linearly with flow rate. For intermediate flow rate, the low and high states are both stable, allowing the system to be in either state. In principle these two population-level states could coexist and interact.

This bistable system may also exhibit hysteresis — if the population is in the low density state, increasing the flow rate f past the bistable regime will cause the system to jump up to the high density state. If f is then decreased, the system will not retrace its steps; instead it will remain in the high density state until f falls below the bistable regime, tracing out a loop indicated by the blue arrows in Figure 4A. Hysteresis may have important ecological consequences, possibly functioning as a memory of past phage pressure or providing a switch-like behaviour between “on” and “off” states of the CRISPR system. Not only can the phage-to-bacterium ratio (called VPR) be significantly

different between the two states but spacer composition and diversity can also be quite different (see Figure 4C and Appendix B.5).

Our model exhibits bistability quite generically for large parameter ranges but requires choosing an appropriately steep function for effectiveness (see discussion in Appendix E). Only total bacteria and total phage are plotted in Figure 4, but the other two system variables (ν and C) also change because of bistability (see Appendix E.2).

4 Discussion

CRISPR-Cas is a unique system in that adaptive immunity is both hereditary and acquired. Its impacts on population dynamics are thus unlike any other immune system, and experimental observations must be interpreted with theory specific to the CRISPR-Cas system. Our analysis of experimental data yielded a striking result: distributions of spacer abundance are stable over time paralleling population-level stability, despite what looks like ongoing turnover in the abundances of individual spacer types. This overall stability suggests a need for a population-level approach in which questions about spacer diversity are addressed alongside questions about CRISPR-Cas regulation. In this framework, communities of bacteria function collectively more like a *single organism* capable of complex signalling and behaviour than like a collection of individual bacteria undergoing selective dynamics.

In this work, we propose and analyze a simplified model of interacting bacteria and phage in which bacteria regulate the CRISPR-Cas system in a density-dependent way, which in turn controls the spacer-marked *clonal* composition of the bacterial population under phage attack. We find that the bacteria-phage population exhibits bistability with the possibility of co-existence between two ecologically different states. These two stable states may differ by orders of magnitude in terms of number of phages per bacterium as well as differing in the spacer diversity and composition of the population. Our model also provides a framework where large variability in spacer abundance may arise due to population dynamics rather than due to individual parameters of spacers. And finally, our model shows how a stable spacer abundance distribution may emerge while individual spacer types turnover rapidly.

Multistability at the level of cellular states, where a fraction of the population switches to an alternate state, has been explored at length with implications from bet-hedging to lytic-lysogenic switching to antibiotic resistance and persistence [43, 44, 45, 46, 47]. Similarly-structured populations are now being explored in contexts from healthy regenerating tissues to pathologies such as cancer [48]. While recent models for large interacting microbial populations using a statistical mechanical approach [49, 50, 51, 52] show that ecological multistability akin to what is seen in a spin glass may be present in such populations, they remain experimentally inaccessible. Here we provide one of the first examples of multistable ecological states that may be readily accessible in experiments. We show that for a population of bacteria and phages the flow rate of a chemostat or dilution rate of a serially diluted population can serve as a bifurcation parameter. To ensure that cell densities are in the appropriate range for quorum sensing to regulate CRISPR-Cas system, the nutrient concentration can be adjusted. Since both nutrient concentration and dilution rate are easy to control experimentally, ecological states in our phage-bacteria population should be readily accessible (see Appendix E.4 for further discussion).

In natural populations, multiple states may define different ecological niches as seen in structured populations from hot spring microbial mats [53] to the human microbiome [54]. Biofilms are an example of both dense and structured communities of bacteria and are found in almost all natural environments such as hot springs [53] and acid mine drainage [6] and in many clinically relevant environments such as medical implants, lungs of cystic fibrosis patients, and dental plaques [55]. Because of their protective polysaccharide coating, biofilms are often difficult to treat with antibiotics [55], and phage therapy has been proposed as a potential treatment for bacterial colonies that are resistant to antibiotics. Høyland-Kroghsbo *et al.* posited that upregulation of CRISPR-Cas in biofilms

could pose a challenge to potential phage therapies for biofilms [28]. If such a biofilm-bound population is in the bistable regime we find, there may be a way to prime the population in way that pushes the population to the low CRISPR-Cas expression state and utilize phage therapy effectively. More broadly, in a resource-limited environment, for example, a bacterial population may do better to maintain a low density and avoid phage predation while repressing the expression of Cas proteins, but consequently may lose their CRISPR-Cas system entirely. These ecological constraints may shed light on why CRISPR-Cas is neither universal nor uncommon in the microbial world.

Sequencing provides an easy way to track spacers, which in turn provide a direct record of past interactions between a bacterium and its phages. Although there has not been much effort at looking at spacers in individual bacteria, population-level spacer dynamics is becoming readily accessible both from laboratory experiments [1, 9, 21] and natural populations [8, 6]. In the laboratory, both large variability and rapid turnover of individual spacer types have been observed. Understanding these dynamics is certainly interesting but requires much higher sampling and resolution than what is currently available [56]. On the other hand, acquiring such data, especially time-resolved, for natural systems such as microbial mats and acid mine drainage may not be practical. Here we show that spacer abundance distribution may provide a more useful time-invariant observable for understanding the underlying dynamics in both natural and laboratory systems.

Even without phage diversity and phage mutations in our model, we reproduce important features of the spacer dynamics observed in recent laboratory experiments that access the co-evolutionary dynamics of bacteria and phages on the population level [1]. In the presence of mutant phages, the net effectiveness of different spacers in providing immunity against phages may vary from one spacer to the next. We expect that a spacer’s effectiveness will depend on the fraction of the phage population with a matching protospacer. This fitness difference between spacers will have consequences for the population dynamics, and some aspects have been addressed in experiments [57, 39, 9] and models [35, 15, 58, 17, 16, 37, 21] and reviewed in [59].

The phage-to-bacterium ratio, also called virus-to-prokaryote ratio (VPR), in natural environments has been measured and reported for a wide range of conditions, and while viruses are generally assumed to outnumber bacteria by a factor of approximately ten [62, 63, 64, 25], the measured ratio can vary between samples by as much as a factor of 10^6 [60]. The underlying factors that determine VPR are not well understood, and interpreting the ecological significance of an observed VPR is also not straightforward. Our model predicts a variable phage-to-bacterium ratio for different parameters. Notably, the VPR for the low-expression branch of the bistable system is approximately ten times higher than for the high-expression branch (Figure 5A). These two VPR values reflect the two underlying ecological states: VPR is low when bacteria are at high density and upregulate CRISPR-Cas expression, and VPR is high when bacteria are at low density and have turned down CRISPR-Cas expression. Since observed VPR values in nature can vary by several orders of magnitude, this suggests that low VPR may be indicative of an active bacterial defense system while high VPR corresponds to a bacterial population strongly controlled by phages.

The relationship between VPR and flow rate in our model also contains a relationship between VPR and nutrient availability: the normalized flow rate f is inversely proportional to the inflow nutrient concentration C_0 , and so increasing f corresponds to decreasing nutrient availability and decreasing bacterial density in the absence of phages. At high f and correspondingly at low nutrient availability, CRISPR provides minimal benefit to bacteria in terms of increased population size, and at very high f , phages cannot persist at all. At low-to-intermediate f and correspondingly intermediate nutrient availability, both regulation strategies can persist (Figure 5A). This suggests that the ecological conditions under which CRISPR-Cas is advantageous may be significantly impacted by nutrient availability, and indeed a study by Payet and Suttle [65] found that phage production and phage-induced mortality of bacteria were both highest in marine samples when the water was most productive and nutrient-rich, while lysogens were more common when the water was oligotrophic. This is also consistent with the finding that phage infection risk is higher at high bacterial density [66, 67, 28].

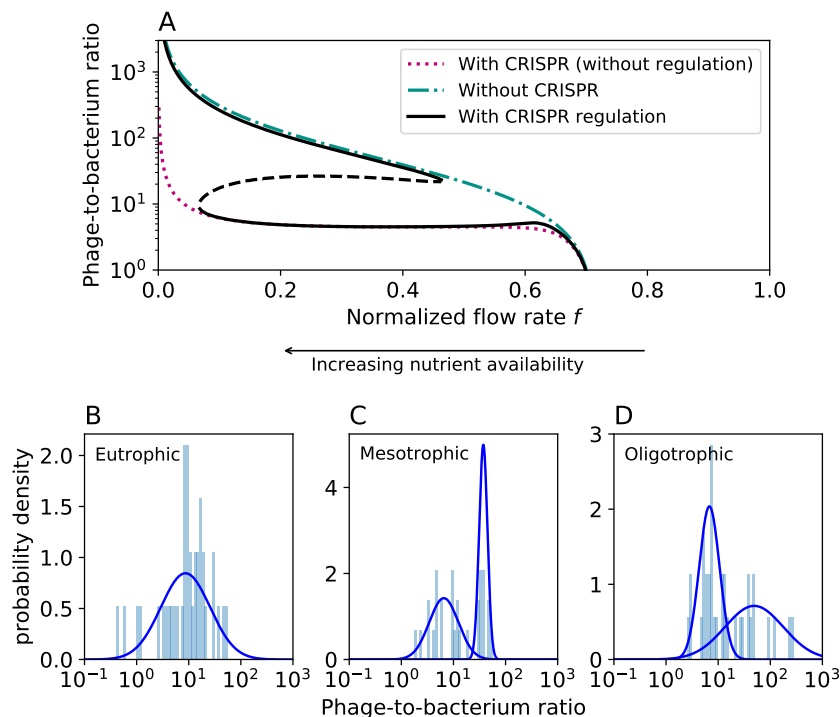


Figure 5: (A) The phage-to-bacterium ratio (virus-to-prokaryote ratio, VPR) can differ by more than ten-fold between the two bistable states in the model (solid black lines). These values reflect the two underlying ecological states: VPR is low when bacteria are at high density and upregulate CRISPR-Cas expression, and VPR is high at low bacterial density and low CRISPR-Cas expression. (B)-(D) VPR histogram and fitted log-normal distributions for organisms from eutrophic (high nutrient), mesotrophic (moderate nutrient), and oligotrophic (low nutrient) environments. Dataset and annotations were assembled by Parikka *et al.* [60]. We fit one-dimensional Gaussian mixture models with one and two Gaussian distributions respectively to the data and chose the best-fitting model using the Akaike Information Criterion (AIC). (B) The eutrophic data was fit better by a single Gaussian distribution (blue line) than two Gaussian distributions ($\Delta \text{AIC} = 45.7$). The relative likelihood that the two-Gaussian model is a better fit is $e^{-\Delta \text{AIC}/2} = 1.2 \times 10^{-10}$ [61]. (C) The mesotrophic data was fit better by two Gaussian distributions than by a single Gaussian distribution ($\Delta \text{AIC} = 10.2$). The relative likelihood that the single-Gaussian model is a better fit is 0.006. (D) The oligotrophic data was fit better by two Gaussian distributions than by a single Gaussian distribution ($\Delta \text{AIC} = 8.1$). The relative likelihood that the single-Gaussian model is a better fit is 0.017.

To connect the qualitative feature of our model to natural populations, we analyzed VPR data from Parikka *et al.* and found that in environments with low and moderate nutrients (oligotrophic and mesotrophic respectively) the VPR distribution is bimodal, while in environments with high nutrients (eutrophic), the VPR distribution is unimodal. This distinction along boundaries of nutrient availability is particularly interesting in light of our result that bistability occurs at intermediate nutrient availability. It may be the case that at high nutrient levels where bacteria live in dense communities and are at high risk of lytic phage predation, most or all bacteria employ a highly-expressed CRISPR-Cas system and VPR is peaked at a single low value in that environment (Figure 5B). Conversely, at low to moderate nutrient levels, different bacteria may use different immune strategies and so VPR values may span a wider range in similar environments (Figure 5C-D). Note that at very low f and high nutrient availability, our model predicts monostability in the low-density, low-expression stable state corresponding to high VPR, yet we observe a unimodal low VPR in high nutrient environments (Figure 5B). In these conditions when phages are a large threat, bacteria may use another signal besides density to upregulate the CRISPR-Cas system. In this work we provide an intuitive connection between an observed quantity such as VPR and a non-trivial insight into the ecological state of interacting bacteria and phages.

5 Methods and Materials

Data Analysis

We analyzed data from an experiment in which *S. thermophilus* bacteria were mixed with phages and sequenced to track the expanding portion of the CRISPR locus over fifteen days [1] by labelling spacers with a type i corresponding to a unique spacer sequence, a locus position j , and a bacteria label k . All spacers within an edit distance of 2 from each other were grouped into the same type). We organized spacer counts into an array s_{ijk} (Equation 1). See Appendix A for details.

Model Analysis

The mean-field model (Equations 2 to 5) were solved exactly at steady state in Mathematica and plotted for different parameter values (Figure 2). Steady-state values with regulation added were calculated numerically. See Appendix C for stability analysis.

Simulations

Simulations were written in C++ and performed using the tau leaping method [68]. See Appendix B.3 for details.

6 Acknowledgments

We thank Devaki Bhaya and Anton Zilman for helpful discussions. We acknowledge funding from the Natural Sciences and Engineering Research Council of Canada and Vanier Canada Graduate Scholarships.

References

- [1] David Paez-Espino, Wesley Morovic, Christine L Sun, Brian C Thomas, Ken-ichi Ueda, Buffy Stahl, Rodolphe Barrangou, and Jillian F Banfield. Strong bias in the bacterial CRISPR elements that confer immunity to phage. *Nature communications*, 4:1430, jan 2013.

- [2] Ruslan Medzhitov and Charles A. Jr Janeway. Innate immunity: the virtues of a nonclonal system of recognition. *Cell*, 91(3):295–298, 1997.
- [3] Simon J Labrie, Julie E Samson, and Sylvain Moineau. Bacteriophage resistance mechanisms. *Nature reviews. Microbiology*, 8(5):317–327, may 2010.
- [4] Wenyan Jiang, Inbal Maniv, Fawaz Arain, Yaying Wang, Bruce R Levin, and Luciano A Marraffini. Dealing with the evolutionary downside of CRISPR immunity: bacteria and beneficial plasmids. *PLoS genetics*, 9(9):e1003844, jan 2013.
- [5] Sylvain Gandon, Pedro F Vale, Guillaume Lafforgue, Francois Gatchitch, Rozenn Gardan, and Sylvain Moineau. Costs of CRISPR-Cas-mediated resistance in *Streptococcus thermophilus*. *Proc Biol Sci*, 282(1812):20151270, 2015.
- [6] Anders F Andersson and Jillian F Banfield. Virus population dynamics and acquired virus resistance in natural microbial communities. *Science (New York, N.Y.)*, 320(5879):1047–50, may 2008.
- [7] Gene W. Tyson and Jillian F. Banfield. Rapidly evolving CRISPRs implicated in acquired resistance of microorganisms to viruses. *Environmental Microbiology*, 10(1):200–207, jan 2008.
- [8] John F Heidelberg, William C Nelson, Thomas Schoenfeld, and Devaki Bhaya. Germ warfare in a microbial mat community: CRISPRs provide insights into the co-evolution of host and viral genomes. *PloS one*, 4(1):e4169, jan 2009.
- [9] David Paez-Espino, Itai Sharon, Wesley Morovic, Buffy Stahl, Brian C Thomas, Rodolphe Barrangou, and Jillian F Banfield. CRISPR Immunity Drives Rapid Phage Genome Evolution in *Streptococcus thermophilus*. *mBio*, 6(2):1–9, 2015.
- [10] Joshua A Weinstein, Ning Jiang, R. A. White, Daniel S Fisher, and Stephen R Quake. High-Throughput Sequencing of the Zebrafish Antibody Repertoire. *Science*, 324(5928):807–810, 2009.
- [11] Veronika I Zarnitsyna, Brian D Evavold, Louis N Schoettle, Joseph N Blattman, and Rustom Antia. Estimating the diversity, completeness, and cross-reactivity of the T cell repertoire. *Frontiers in Immunology*, 4(DEC):1–11, 2013.
- [12] Jonathan Desponds, Thierry Mora, and Aleksandra M Walczak. Fluctuating fitness shapes the clone-size distribution of immune repertoires. *Proceedings of the National Academy of Sciences of the United States of America*, 113(2):274–9, jan 2016.
- [13] Stineke van Houte, Alice K.E. Ekroth, Jenny M. Broniewski, Hélène Chabas, Ben Ashby, Sylvain Gandon, Steve Paterson Mike Boots⁴, Angus J. Buckling, and Edze R. Westra. The diversity-generating benefits of a prokaryotic adaptive immune system. *Nature*, 532(7599):385–388, 2016.
- [14] Silja Heilmann, Kim Sneppen, and Sandeep Krishna. Sustainability of virulence in a phage-bacterial ecosystem. *Journal of virology*, 84(6):3016–22, 2010.
- [15] Ariel D Weinberger, Yuri I Wolf, Alexander E Lobkovsky, Michael S Gilmore, and Eugene V Koonin. Viral diversity threshold for adaptive immunity in prokaryotes. *mBio*, 3(6):1–10, 2012.
- [16] Jaime Iranzo, Alexander E Lobkovsky, Yuri I Wolf, and Eugene V. Koonin. Evolutionary dynamics of the prokaryotic adaptive immunity system CRISPR-Cas in an explicit ecological context. *Journal of Bacteriology*, 195(17):3834–3844, 2013.
- [17] Bruce R. Levin, Sylvain Moineau, Mary Bushman, and Rodolphe Barrangou. The Population and Evolutionary Dynamics of Phage and Bacteria with CRISPR-Mediated Immunity. *PLoS Genetics*, 9(3):e1003312, jan 2013.

- [18] Faina S Berezovskaya, Yuri I Wolf, Eugene V Koonin, and Georgy P Karev. Pseudo-chaotic oscillations in CRISPR-virus coevolution predicted by bifurcation analysis. *Biology Direct*, 9(1):13, 2014.
- [19] Serena Bradde, Marija Vucelja, Tiberiu Tesileanu, and Vijay Balasubramanian. Dynamics of adaptive immunity against phage in bacterial populations. *PNAS*, I(1):1–6, 2015.
- [20] Pu Han and Michael W Deem. Non-classical phase diagram for virus bacterial coevolution mediated by clustered regularly interspaced short palindromic repeats. *Journal of The Royal Society Interface*, 14(127):20160905, 2017.
- [21] Jake L Weissman, Rayshawn Holmes, Rodolphe Barrangou, Sylvain Moineau, William F Fagan, Bruce Levin, and Philip LF Johnson. Immune Loss as a Driver of Coexistence During Host-Phage Coevolution. *bioRxiv*, page 105908, 2017.
- [22] Bruce R Levin. Nasty viruses, costly plasmids, population dynamics, and the conditions for establishing and maintaining CRISPR-mediated adaptive immunity in bacteria. *PLoS genetics*, 6(10):e1001171, oct 2010.
- [23] Edze R Westra, Stineke Van houte, Sam Oyesiku-Blakemore, Ben Makin, Jenny M Broniewski, Alex Best, Joseph Bondy-Denomy, Alan Davidson, Mike Boots, and Angus Buckling. Parasite exposure drives selective evolution of constitutive versus inducible defense. *Current Biology*, 25(8):1043–1049, 2015.
- [24] Qasim Ali and Lindi M. Wahl. Mathematical modelling of CRISPR-Cas system effects on biofilm formation. *Journal of Biological Dynamics*, 11(October):264–284, 2017.
- [25] Sílvia B. Santos, Carla Carvalho, Joana Azeredo, and Eugénio C. Ferreira. Population dynamics of a Salmonella lytic phage and its host: Implications of the host bacterial growth rate in modelling. *PLoS ONE*, 9(7), 2014.
- [26] Jan O Haerter, Ala Trusina, and Kim Sneppen. Targeted Bacterial Immunity Buffers Phage Diversity. *Journal of Virology*, 85(20):10554–10560, 2011.
- [27] Jan O Haerter and Kim Sneppen. Spatial structure and Lamarckian adaptation explain extreme genetic diversity at CRISPR locus. *mBio*, 3(4):1–6, 2012.
- [28] Nina M Høyland-Krogsho, Jon Paczkowski, Sampriya Mukherjee, Jenny Broniewski, Edze Westra, Joseph Bondy-Denomy, and Bonnie L Bassler. Quorum sensing controls the *Pseudomonas aeruginosa* CRISPR-Cas adaptive immune system. *Proceedings of the National Academy of Sciences of the United States of America*, 114(1):201617415, 2016.
- [29] Adrian G Patterson, Simon A Jackson, Corinda Taylor, Rita Przybilski, Raymond H J Staals, Peter C Fineran, Adrian G Patterson, Simon A Jackson, Corinda Taylor, Gary B Evans, George P C Salmond, Rita Przybilski, Raymond H J Staals, and Peter C Fineran. Quorum Sensing Controls Adaptive Immunity through the Regulation of Multiple CRISPR-Cas Systems. *Molecular Cell*, 64(6):1102–1108, 2016.
- [30] Marko Djordjevic, Magdalena Djordjevic, and Konstantin Severinov. CRISPR transcript processing: a mechanism for generating a large number of small interfering RNAs. *Biology Direct*, 7(1):24, 2012.
- [31] Marko Djordjevic. Modeling bacterial immune systems : Strategies for expression of toxic but useful molecules. *BioSystems*, 112(2):139–144, 2013.

- [32] Jelena Guzina, Anela Rodić, Bojana Blagojević, and Marko orević. Modeling and bioinformatics of bacterial immune systems: understanding regulation of CRISPR/Cas and restriction-modification systems. *Biologia Serbica*, 39(1):112–122, 2017.
- [33] Jiankui He and Michael W. Deem. Heterogeneous Diversity of Spacers within CRISPR (Clustered Regularly Interspaced Short Palindromic Repeats). *Physical Review Letters*, 105(12):128102, sep 2010.
- [34] Ariel D Weinberger, Christine L Sun, Mateusz M Pluciński, Vincent J Deneff, Brian C Thomas, Philippe Horvath, Rodolphe Barrangou, Michael S Gilmore, Wayne M Getz, and Jillian F Banfield. Persisting viral sequences shape microbial CRISPR-based immunity. *PLoS computational biology*, 8(4):e1002475, jan 2012.
- [35] Lauren M Childs, Nicole L Held, Mark J Young, Rachel J Whitaker, and Joshua S Weitz. Multiscale model of CRISPR-induced coevolutionary dynamics: diversification at the interface of Lamarck and Darwin. *Evolution; international journal of organic evolution*, 66(7):2015–29, jul 2012.
- [36] Pu Han, Liang Ren Niestemski, Jeffrey E. Barrick, and Michael W. Deem. Physical Model of the Immune Response of Bacteria Against Bacteriophage Through the Adaptive CRISPR-Cas Immune System. *Physical Biology*, 10(025004):025004, apr 2013.
- [37] Lauren M Childs, Whitney E England, Mark J Young, Joshua S Weitz, and Rachel J Whitaker. CRISPR-induced distributed immunity in microbial populations. *PLoS ONE*, 9(7):1–12, 2014.
- [38] Serena Bradde, Marija Vucelja, Tiberiu Teileanu, and Vijay Balasubramanian. Dynamics of adaptive immunity against phage in bacterial populations. *PLoS Computational Biology*, 13(4):1–16, 2017.
- [39] Christine L. Sun, Rodolphe Barrangou, Brian C. Thomas, Philippe Horvath, Christophe Fremaux, and Jillian F. Banfield. Phage mutations in response to CRISPR diversification in a bacterial population. *Environmental Microbiology*, 15(2):463–470, feb 2013.
- [40] Rodolphe Barrangou and Luciano A. Marraffini. CRISPR-cas systems: Prokaryotes upgrade to adaptive immunity. *Molecular Cell*, 54(2):234–244, apr 2014.
- [41] Joanne B. Emerson, Karen Andrade, Brian C. Thomas, Anders Norman, Eric E. Allen, Karla B. Heidelberg, and Jillian F. Banfield. Virus-host and CRISPR dynamics in archaea-dominated hypersaline Lake tyrrell, Victoria, Australia. *Archaea*, 2013, 2013.
- [42] David T Pride, Christine L Sun, Julia Salzman, Nitya Rao, Peter Loomer, Gary C Armitage, Jillian F Banfield, and David A Relman. Analysis of streptococcal CRISPRs from human saliva reveals substantial sequence diversity within and between subjects over time. *Genome research*, 21(1):126–36, jan 2011.
- [43] Jeff Gore, Hyun Youk, and Alexander Van Oudenaarden. Snowdrift game dynamics and facultative cheating in yeast. *Nature*, 459(7244):253–256, 2009.
- [44] Avigdor Eldar and Michael B Elowitz. Functional roles for noise in genetic circuits. *Nature*, 467(7312):167–173, 2010.
- [45] Thomas M Norman, Nathan D Lord, Johan Paulsson, and Richard Losick. Stochastic Switching of Cell Fate in Microbes. *Annual Review of Microbiology*, 69(1):381–403, 2015.
- [46] Corina E Tarnita, Alex Washburne, Ricardo Martinez-Garcia, Allyson E Sgro, and Simon a Levin. Fitness tradeoffs between spores and nonaggregating cells can explain the coexistence of diverse genotypes in cellular slime molds. *Proceedings of the National Academy of Sciences of the United States of America*, 112(9):2776–81, 2015.

- [47] Orsolya Symmons and Arjun Raj. What’s Luck Got to Do with It: Single Cells, Multiple Fates, and Biological Nondeterminism. *Molecular Cell*, 62(5):788–802, 2016.
- [48] Sydney M Shaffer, Margaret C Dunagin, Stefan R Torborg, Eduardo A Torre, Benjamin Emert, Clemens Krepler, Marilda Beqiri, Katrin Sproesser, Patricia A Brafford, Min Xiao, Elliott Eggan, Ioannis N Anastopoulos, Cesar A. Vargas-Garcia, Abhyudai Singh, Katherine L Nathanson, Meenhard Herlyn, and Arjun Raj. Rare cell variability and drug-induced reprogramming as a mode of cancer drug resistance. *Nature*, 546(7658):431–435, 2017.
- [49] Guy Bunin. Interaction patterns and diversity in assembled ecological communities. *arXiv*, 2016.
- [50] Mikhail Tikhonov. Community-level cohesion without cooperation. *eLife*, 5(JUN2016):1–15, 2016.
- [51] Mikhail Tikhonov and Remi Monasson. Collective Phase in Resource Competition in a Highly Diverse Ecosystem. *Physical Review Letters*, 118(4):1–5, 2017.
- [52] Giulio Biroli, Guy Bunin, and Chiara Cammarota. Marginally Stable Equilibria in Critical Ecosystems. *arXiv*, 2017.
- [53] David M Ward, Mary M Bateson, Michael J Ferris, M. Kuhl, Andrea Wieland, Alex Koeppl, and Frederick M Cohan. Cyanobacterial ecotypes in the microbial mat community of Mushroom Spring (Yellowstone National Park, Wyoming) as species-like units linking microbial community composition, structure and function. *Philosophical Transactions of the Royal Society B: Biological Sciences*, 361(1475):1997–2008, 2006.
- [54] Curtis Huttenhower et al. Structure, function and diversity of the healthy human microbiome. *Nature*, 486(7402):207–214, jun 2012.
- [55] Michael T. Madigan, Michael T. Madigan, and Thomas D. Brock. *Brock biology of microorganisms*. 2009.
- [56] Sasha F. Levy, Jamie R. Blundell, Sandeep Venkataram, Dmitri A. Petrov, Daniel S. Fisher, and Gavin Sherlock. Quantitative evolutionary dynamics using high-resolution lineage tracking. *Nature*, 519(7542):181–186, feb 2015.
- [57] Hélène Deveau, Rodolphe Barrangou, Josiane E. Garneau, Jessica Labonté, Christophe Fremaux, Patrick Boyaval, Dennis a. Romero, Philippe Horvath, and Sylvain Moineau. Phage response to CRISPR-encoded resistance in *Streptococcus thermophilus*. *Journal of Bacteriology*, 190(4):1390–1400, feb 2008.
- [58] Pu Han, Liang Ren Niestemski, Jeffrey E Barrick, and Michael W Deem. Physical model of the immune response of bacteria against bacteriophage through the adaptive CRISPR-Cas immune system. *Physical biology*, 10(2):025004, apr 2013.
- [59] Whitney E. England and Rachel J. Whitaker. Evolutionary causes and consequences of diversified CRISPR immune profiles in natural populations. *Biochemical Society Transactions*, 41(6):1431–1436, 2013.
- [60] Kaarle J Parikka, Marc Le Romancer, Nina Wauters, and Stéphan Jacquet. Deciphering the virus-to-prokaryote ratio (VPR): Insights into virus-host relationships in a variety of ecosystems, 2017.
- [61] K.P. Burnham and D.R. Anderson. *Model Selection and Multimodel Inference: A Practical Information-Theoretic Approach (2nd ed)*, volume 172. 2002.

- [62] Harald Brüssow and Roger W. Hendrix. Phage Genomics: Small is beautiful. *Cell*, 108(1):13–16, jan 2002.
- [63] Curtis A Suttle. Marine viruses—major players in the global ecosystem. *Nature reviews. Microbiology*, 5(10):801–812, 2007.
- [64] Nicole L Held, Lauren M Childs, Michelle Davison, Joshua S Weitz, Rachel J Whitaker, and Devaki Bhaya. CRISPR-Cas systems to probe ecological diversity and host-viral interactions. In *CRISPR-Cas Systems: RNA-Mediated Adaptive Immunity in Bacteria and Archaea*, pages 221–250. 2013.
- [65] Jérôme P. Payet and Curtis A Suttle. To kill or not to kill: The balance between lytic and lysogenic viral infection is driven by trophic status. *Limnology and Oceanography*, 58(2):465–474, 2013.
- [66] Laura M Kasman, Alex Kasman, Caroline Westwater, Joseph Dolan, Michael G Schmidt, and James S Norris. Overcoming the phage replication threshold: a mathematical model with implications for phage therapy. *Journal of virology*, 76(11):5557–64, 2002.
- [67] B Knowles, C B Silveira, B A Bailey, K Barott, V A Cantu, A. G. Cobian-Guêmes, F H Coutinho, E A Dinsdale, B Felts, K A Furby, E E George, K T Green, G B Gregoracci, A F Haas, J M Haggerty, E R Hester, N Hisakawa, L W Kelly, Y W Lim, M Little, A Luque, T. McDole-Somera, K. McNair, L. S. De Oliveira, S D Quistad, N L Robinett, E Sala, P Salamon, S E Sanchez, S Sandin, G. G.Z. Silva, J Smith, C Sullivan, C. Thompson, M. J.A. Vermeij, M Youle, C Young, B Zgliczynski, R Brainard, R A Edwards, J Nulton, F Thompson, and F Rohwer. Lytic to temperate switching of viral communities. *Nature*, 531(7595):466–470, 2016.
- [68] Yang Cao, Daniel T. Gillespie, and Linda R. Petzold. Efficient step size selection for the tau-leaping simulation method. *The Journal of chemical physics*, 124(4):044109, 2006.
- [69] André Gilles, Emese Megléc, Nicolas Pech, Stéphanie Ferreira, Thibaut Malausa, and Jean-françois Martin. Accuracy and quality assessment of 454 GS-FLX Titanium pyrosequencing. *BMC Genomics*, 12(1):245, 2011.
- [70] Sacha Lucchini. *Genetic Diversity of Streptococcus thermophilus Phages and Development of*. PhD thesis, 1999.
- [71] M Delbrück. Adsorption of bacteriophage under various physiological conditions of the host. *The Journal of general physiology*, 23(5):631–42, 1940.
- [72] F. Vaningelgem, M. Zamfir, T. Adriany, and Luc De Vuyst. Fermentation conditions affecting the bacterial growth and exopolysaccharide production by *Streptococcus thermophilus* ST 111 in milk-based medium. *Journal of Applied Microbiology*, 97(6):1257–1273, 2004.
- [73] Melissa B Miller and Bonnie L Bassler. Quorum Sensing in Bacteria. *Annual Review of Microbiology*, 55(1):165–199, 2001.

A Data analysis

We used data from [1] which is publicly available in the NCBI Sequence Read Archive under the accession SRA062737. It includes four data files (SRR630110, SRR630111, SRR630412, and SRR630413) which we used for our analysis. We extracted the data corresponding to the MOI2 deep sequencing experiment and separated it into time points by checking each read for matches to the primers identified in the supplementary information of [1]. Any reads with a mismatch between the annotation of the forward and reverse primers were discarded. Any remaining unsorted reads were excluded from the following analysis.

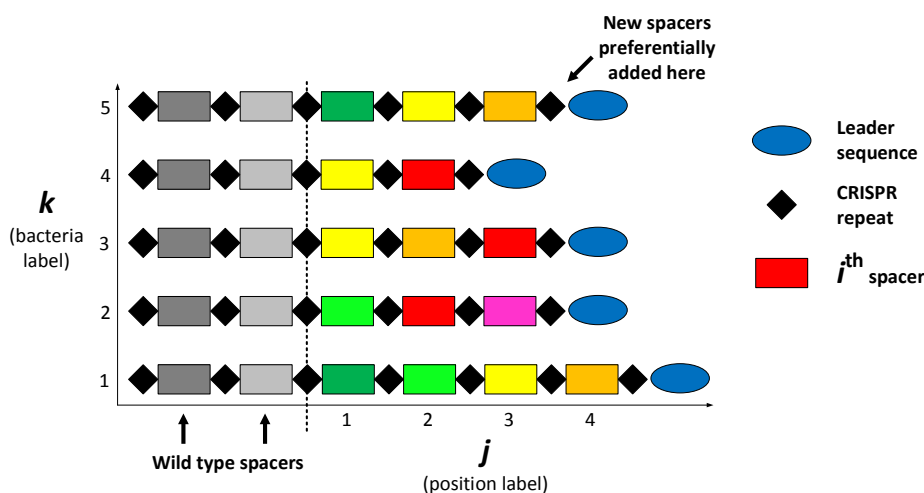


Figure 6: Schematic of the portion of the *S. thermophilus* CRISPR locus sequenced in [1]. We identified spacers with a type i , a locus position j , and bacteria number k . Coloured rectangles to the right of the dashed line represent spacers sequenced as the locus expands. Wild type spacers are shown in greyscale.

```

ATCAGACACGGAAAGTAAGGATTGACAAGGACAGTTATTGATTTTATAATCACTATGTGGGTATAA
AACGTC AAGATTTTATTGAGGTTTTGTACTCTCAAGATTTAAGTAACTGTACAACCCAACTC
AAACGTTGCAAACGCAAGCTTGTTTTGTACTCTCAAGATTTAAGTAACTGTACAACATCACTTAC
GAGGTTGACGGTTTTGTAGATGTTTTGTACTCTCAAGATTTAAGTAACTGTACAACTGTTTGACA
GCAAATCAAGCGTGTCTGATCTGAGCGGGCTGGCAAGGCGCATAGN

```

CRISPR repeat, *forward primer*, *reverse primer*, *spacer*

Figure 7: Example read covering the expanding CRISPR locus. The forward primer which overlaps with the leader sequence is shown in blue italics. The reverse primer which overlaps the first wild type spacer is shown in green italics. CRISPR repeats are shown in bold red and spacers in bold black.

A.1 Identifying and sorting spacers

We extracted and catalogued spacers from the published raw read data of [1]. Since only the expanding CRISPR end was sequenced, each read represents the longest possible sequence from wild type to leader end and so further assembly was not required (Fig. 6 and Fig. 7).

Because of this very specialized data structure, detecting CRISPR spacers and inferring their order was conceptually straightforward. A spacer was defined as any sequence flanked by two repeats. Since each read was bordered by wild type sequence and leader end sequence, all repeat sequences were complete and not truncated. Figure 7 shows a typical read in more detail. Note that in this orientation, the spacer numbered “1” is found at the end of the read. To collect spacers, we (1) detected repeat sequences, reversing the read if the repeats were reversed, (2) inferred spacers as sequences between repeats, and (3) categorized spacers by comparing to previously detected spacers.

Repeat sequence variation was present due to sequencing errors or naturally occurring SNPs. We used a regular expression to match variations on the number of Ts in a 5-T region of the repeat - the forward repeat was matched with “GTTT*GTACTCTCAAGATTTAAGTAACTGTACAAC” and the reverse repeat was matched with “GTTGTACAGTTACTTAAATCTTGAGAGTACAAA*C”. These

expressions match an identical string with three or more Ts or As in the region of the asterisk. This is a reasonable allowance to make since the 454 sequencing platform used to sequence this data is known to have high insertion and deletion rates in homopolymer regions [69].

To detect the most possible spacers, we developed methods to deal with repeat sequence variation beyond simple insertions and deletions in the homopolymer region. We inferred the presence of an undetected repeat by measuring the length of sequence before the first detected repeat, after the last detected repeat, and between two repeats. If any of these lengths exceeded its threshold (determined based on the known primer lengths and average spacer length, respectively), a more careful search for repeats was performed using the *pairwise2* module in Biopython which performs a local pairwise alignment between the ideal repeat sequence and the read in question.

A.1.1 Pairwise alignment settings

If the alignment with the true repeat (36 nucleotides long) was less than 31 nucleotides long, the alignment was discarded. The scoring system was as follows: match score of 1, mismatch score of -1, gap open score of -0.8 for the target sequence, gap open score of -0.7 for the repeat, and gap extend penalty of -1 for each sequence. The gap open scores were chosen to be different for the repeat and read so that the algorithm could identify how many gaps were opened and in which each sequence, in order to properly identify the start and end of each spacer.

If no good match was found in a region between two repeats, the remaining “long” spacer was discarded and a placeholder was inserted to preserve position information. Using this method, the number of detected repeats increased from 550931 to 622067, a 12.9% increase.

Repeats detected in this second search sometimes contained gaps with respect to the read or vice versa. In these cases, conventional labelling of nucleotide position prevented accurate detection of the start and end of adjacent spacers. We detected how many gaps were present and whether they occurred in the repeat or the read and then adjusted the indices of adjacent spacers accordingly. The scoring scheme was carefully chosen so that the number and placement of gaps could be inferred from the score.

A.1.2 Spacer type assignment

We compared newly detected spacers to a growing list of previously detected spacers to assign it a type. If it matched an existing spacer exactly, it was assigned that type. Otherwise, a global pairwise alignment was performed between the new spacer and all existing spacers. If a match was found for which the score subtracted from the spacer length was within a chosen cutoff, the new spacer was assigned that type. This definition of cutoff is equivalent to the number of allowed SNPs between spacers under the scoring scheme used. If no match was found in either case, the new spacer was assigned a new type.

To choose an appropriate tolerance for spacer likeness, we tested this spacer sorting algorithm on a small sample of data (190 reads) as the cutoff was increased from 0 to 9. Fig. 8 shows the number of unique spacer types detected as the cutoff is changed. It can be seen that there is a clear plateau between cutoff values of 1 and 8, which indicates that the system is insensitive to the cutoff if it falls in this range. We chose a cutoff of 2 for the analysis.

In this way, we created a master dataset for each time point that contained each detected spacer, a number indicating the source read, the spacer position in the read, and the assigned spacer type. The definition of spacer type was consistent across time points, or in other words the same comparison list was carried through all time points.

A.2 Analysis

We extracted CRISPR spacers from the raw reads at each time point by finding sequences flanked by an *S. thermophilus* CRISPR repeat (Fig. 6). Newly detected spacers were added to an existing group

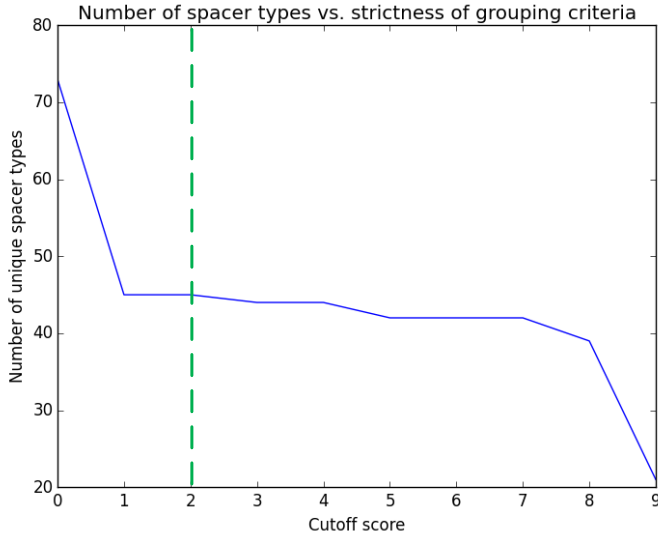


Figure 8: Number of unique spacer types vs. cutoff for 190 reads from time point 11. The green vertical dashed line indicates the selected cutoff.

if they were within an edit distance of 2 of another spacer in that group. Data was organized into an array s_{ijk} (equation 6).

$$s_{ijk}(t) = \begin{cases} 1 & \text{if spacer type } i \text{ is at position } j \text{ in bacterium } k \\ 0 & \text{otherwise} \end{cases} \quad (6)$$

We tracked individual spacer types, or “clones”, $n_B^i(t)$, by summing over all bacteria and all locus positions: $n_B^i(t) = \sum_{j,k} s_{ijk}(t)$.

Most bacteria acquired only a single spacer; over half of bacteria from days 4-14 which had acquired 1 or more spacers only acquired a single spacer (Figure 9).

B Model description

We model bacteria and phages interacting in a chemostat. The populations we track are nutrient concentration C , phages n_V , and bacteria n_b which can either have no spacer (n_b^0) or a spacer of type i (n_b^i). Nutrients flow in at concentration C_0 with rate F , and all species flow out with rate F . The total number of bacteria with a spacer is n_b^s and the total number of bacteria is n_B . The phage in the solution are all clonal and have m distinct protospacers. Bacteria grow at rate gC . With rate α , a phage interacts with a bacterium. With probability p_V , the phage will kill bacteria without spacers and produce a burst of new phages with size B , while for bacteria with spacers that probability is reduced to $p_v^s = (1 - e)p_V$ ($0 \leq e \leq 1$). Bacteria without spacers that survive an attack have a chance to acquire a spacer with probability η . Bacteria with a spacer lose their spacer at rate r .

B.0.1 Reactions

Table 2 lists all the interactions present in our model between individual bacteria (b), phages (V) and nutrients (C).

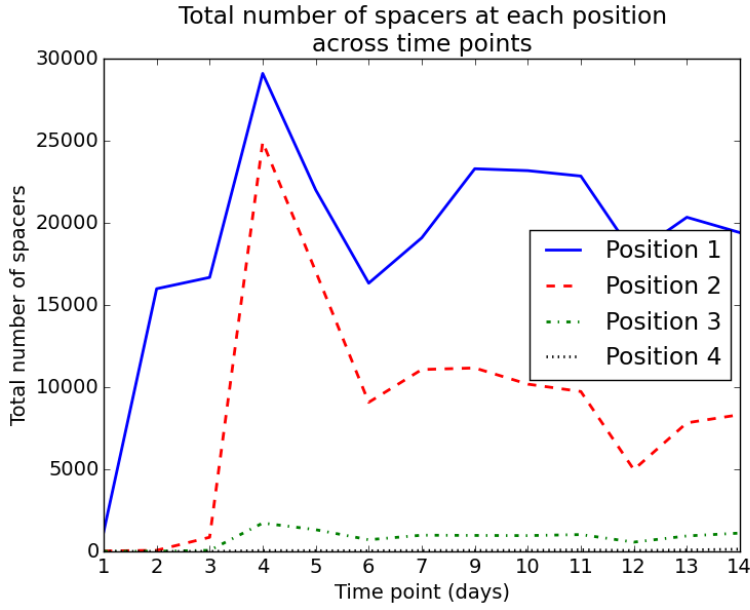


Figure 9: Total number of spacers at each time point in the experiment. Position 1 represents the oldest spacer (closest to the wild type spacers). Over half of all bacteria that acquired spacers, even at the end of the experiment, only acquired a single spacer.

Table 2: Model reactions

$b^{0,i} + C \xrightarrow{g} 2b^{0,i}$	bacterium divides
$b^{0,i} \xrightarrow{F} \emptyset$	bacterium flows out
$V \xrightarrow{F} \emptyset$	phage flows out
$\emptyset \xrightarrow{FC_0} C$	nutrients flow in
$C \xrightarrow{F} \emptyset$	nutrients flow out
$b^0 + V \xrightarrow{\alpha p v} BV$	interaction, phage wins
$b^0 + V \xrightarrow{\alpha(1-pv)(1-\eta)} b^0$	interaction, bacterium survives
$b^0 + V \xrightarrow{\alpha(1-pv)\eta/m} b^i$	interaction, bacterium survives and acquires a spacer
$b^i + V \xrightarrow{\alpha p v^s} BV$	interaction, phage wins
$b^i + V \xrightarrow{\alpha(1-pv^s)} b^i$	interaction, bacterium survives
$b^i \xrightarrow{r} b^0$	bacterium loses spacer

B.1 Master equation

The reactions in Table 2 can be formulated as a master equation describing the probability of observing n_b^0 bacteria without spacers, the set n_b^i bacteria with spacers of type i , n_V phages, and a nutrient concentration of C at time t (equation 7).

$$\begin{aligned}
\frac{dP(n_b^0, \{n_b^i\}, n_V, C, t)}{dt} = & g(C+1)(n_b^0-1)P(n_b^0-1, \{n_b^i\}, n_V, C+1, t) \\
& + \sum_{j=1}^m g(C+1)(n_b^j-1)P(n_b^0, \{n_b^{i \neq j}\}, n_b^j-1, n_V, C+1, t) \\
& + F(n_b^0+1)P(n_b^0+1, \{n_b^i\}, n_V, C, t) \\
& + \sum_{j=1}^m F(n_b^j+1)P(n_b^0, \{n_b^{i \neq j}\}, n_b^j+1, n_V, C, t) \\
& + F(n_V+1)P(n_b^0, \{n_b^i\}, n_V+1, C, t) \\
& + F(C+1)P(n_b^0, \{n_b^i\}, n_V, C+1, t) \\
& + FC_0P(n_b^0, \{n_b^i\}, n_V, C-1, t) \\
& + \alpha p_V(n_b^0+1)(n_V-B+1)P(n_b^0+1, \{n_b^i\}, n_V-B+1, C, t) \\
& + \alpha(1-p_V)(1-\eta)n_b^0(n_V+1)P(n_b^0, \{n_b^i\}, n_V+1, C, t) \\
& + \sum_{j=1}^m \frac{\alpha(1-p_V)\eta}{m}(n_b^0+1)(n_V+1)P(n_b^0+1, \{n_b^{i \neq j}\}, n_b^j-1, n_V+1, C, t) \quad (7) \\
& + \sum_{j=1}^m \alpha p_v^s(n_b^j+1)(n_V-B+1)P(n_b^0, \{n_b^{i \neq j}\}, n_b^j+1, n_V-B+1, C, t) \\
& + \sum_{j=1}^m \alpha(1-p_v^s)n_b^j(n_V+1)P(n_b^0, \{n_b^{i \neq j}\}, n_b^j, n_V+1, C, t) \\
& + \sum_{j=1}^m r(n_b^j+1)P(n_b^0-1, \{n_b^{i \neq j}\}, n_b^j+1, n_V, C, t) \\
& - \left(F(n_b^0 + \sum_{j=1}^m n_b^j + n_V + C + C_0) + gC(n_b^0 + \sum_{j=1}^m n_b^j) \right. \\
& \left. + \alpha n_V(n_b^0 + \sum_{j=1}^m n_b^j) + r \sum_{j=1}^m n_b^j \right) P(n_b^0, \{n_b^i\}, n_V, C, t)
\end{aligned}$$

The 1st term is included only for $n_b^0 > 1$, the 2nd term if $n_b^j > 1$, the 7th term for $C \geq 1$, 8th term if $n_V > B-1$, the 10th term for $n_b^j \geq 1$, the 11th term for $n_V > B-1$ and the 13th term for $n_b^0 \geq 1$.

B.2 Mean-field dynamics

We can also write equations for the averages of the microscopic quantities (equations 8 to 11).

B.2.1 Microscopic equations

$$\frac{d\langle n_b^0 \rangle}{dt} = -F\langle n_b^0 \rangle + g\langle Cn_b^0 \rangle - \alpha p_V\langle n_b^0 n_V \rangle - \alpha(1-p_V)\eta\langle n_b^0 n_V \rangle + \sum_{j=1}^m r\langle n_b^j \rangle \quad (8)$$

$$\frac{d\langle n_b^j \rangle}{dt} = -F\langle n_b^j \rangle + g\langle Cn_b^j \rangle - \alpha p_v^s \langle n_b^j n_V \rangle - r\langle n_b^j \rangle + \frac{\alpha(1-p_V)\eta}{m} \langle n_b^0 n_V \rangle \quad (9)$$

$$\begin{aligned} \frac{d\langle n_V \rangle}{dt} = & -F\langle n_V \rangle + \alpha p_V(B-1)\langle n_b^0 n_V \rangle - \alpha(1-p_V)\langle n_b^0 n_V \rangle + \\ & \sum_{j=1}^m \alpha p_v^s(B-1)\langle n_b^j n_V \rangle - \sum_{j=1}^m \alpha(1-p_v^s)\langle n_b^j n_V \rangle \end{aligned} \quad (10)$$

$$\frac{d\langle C \rangle}{dt} = F(\langle C \rangle - C_0) - g\left\langle C \left(n_b^0 + \sum_{j=1}^m n_b^j \right) \right\rangle \quad (11)$$

We approximate the correlations $\langle XY \rangle \approx \langle X \rangle \langle Y \rangle$.

$$\frac{d\langle n_b^0 \rangle}{dt} = -F\langle n_b^0 \rangle + g\langle C \rangle \langle n_b^0 \rangle - \alpha p_V \langle n_b^0 \rangle \langle n_V \rangle - \alpha(1-p_V)\eta \langle n_b^0 \rangle \langle n_V \rangle + \sum_{j=1}^m r \langle n_b^j \rangle \quad (12)$$

$$\frac{d\langle n_b^j \rangle}{dt} = -F\langle n_b^j \rangle + g\langle C \rangle \langle n_b^j \rangle - \alpha p_v^s \langle n_b^j \rangle \langle n_V \rangle - r\langle n_b^j \rangle + \frac{\alpha(1-p_V)\eta}{m} \langle n_b^0 \rangle \langle n_V \rangle \quad (13)$$

$$\begin{aligned} \frac{d\langle n_V \rangle}{dt} = & -F\langle n_V \rangle + \alpha p_V(B-1)\langle n_b^0 \rangle \langle n_V \rangle - \alpha(1-p_V)\langle n_b^0 \rangle \langle n_V \rangle + \\ & \sum_{j=1}^m \alpha p_v^s(B-1)\langle n_b^j \rangle \langle n_V \rangle - \sum_{j=1}^m \alpha(1-p_v^s)\langle n_b^j \rangle \langle n_V \rangle \end{aligned} \quad (14)$$

$$\frac{d\langle C \rangle}{dt} = F(\langle C \rangle - C_0) - g\langle C \rangle \left(\langle n_b^0 \rangle + \sum_{j=1}^m \langle n_b^j \rangle \right) \quad (15)$$

Then, we replace means by deterministic variables n_b^0 , n_b^j , n_V , and C .

$$\frac{dn_b^0}{dt} = -Fn_b^0 + gCn_b^0 - \alpha p_V n_b^0 n_V - \alpha(1-p_V)\eta n_b^0 n_V + \sum_{j=1}^m r n_b^j \quad (16)$$

$$\frac{dn_b^j}{dt} = -Fn_b^j + gCn_b^j - \alpha p_v^s n_b^j n_V - r n_b^j + \frac{\alpha(1-p_V)\eta}{m} n_b^0 n_V \quad (17)$$

$$\begin{aligned} \frac{dn_V}{dt} = & -Fn_V + \alpha p_V(B-1)n_b^0 n_V - \alpha(1-p_V)n_b^0 n_V \\ & + \sum_{j=1}^m \alpha p_v^s(B-1)n_b^j n_V - \sum_{j=1}^m \alpha(1-p_v^s)n_b^j n_V \end{aligned} \quad (18)$$

$$\frac{dC}{dt} = F(C - C_0) - gC \left(n_b^0 + \sum_{j=1}^m n_b^j \right) \quad (19)$$

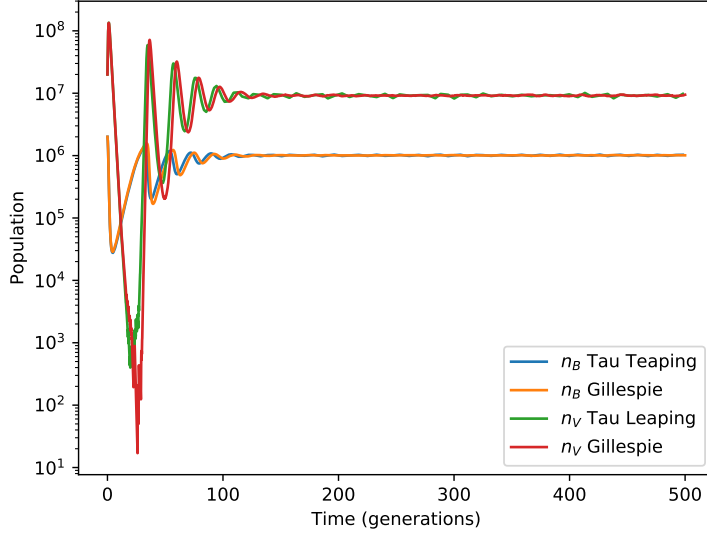


Figure 10: Total bacteria and total phage as a function of time for Gillespie simulations and tau leaping simulations

B.2.2 Macroscopic equations

We can define new variables, $n_b^s = \sum_{j=1}^m n_b^j$, $n_B = n_b^0 + n_b^s$, $\nu = n_b^s/n_B$ ($1 - \nu = n_b^0/n_B$), and $p_V^s = (1 - e)p_V$.

$$\frac{dn_b^0}{dt} = -Fn_b^0 + gCn_b^0 - \alpha p_V n_b^0 n_V - \alpha(1 - p_V)\eta n_b^0 n_V + rn_b^s \quad (20)$$

$$\frac{dn_b^s}{dt} = -Fn_b^s + gCn_b^s - \alpha(1 - e)p_V n_b^s n_V - rn_b^s + \alpha(1 - p_V)\eta n_b^0 n_V \quad (21)$$

$$\frac{dn_V}{dt} = -Fn_V - \alpha n_B n_V + \alpha p_V(1 - e\nu)Bn_B n_V \quad (22)$$

$$\frac{dC}{dt} = F(C - C_0) - gCn_B \quad (23)$$

$$\frac{dn_B}{dt} = -Fn_B + gCn_B - \alpha p_V(1 - e\nu)n_B n_V \quad (24)$$

B.3 Description of simulations

Simulations were written in C++ and performed on a Lenovo ideapad Y700 and on SciNet. We primarily used the tau leaping method [68] and compared with Gillespie simulations for some cases. Both methods showed good agreement for the mean-field behaviour of bacteria and phages (Figure 10) and produced the same qualitative behaviour for individual spacer types (Figure 11).

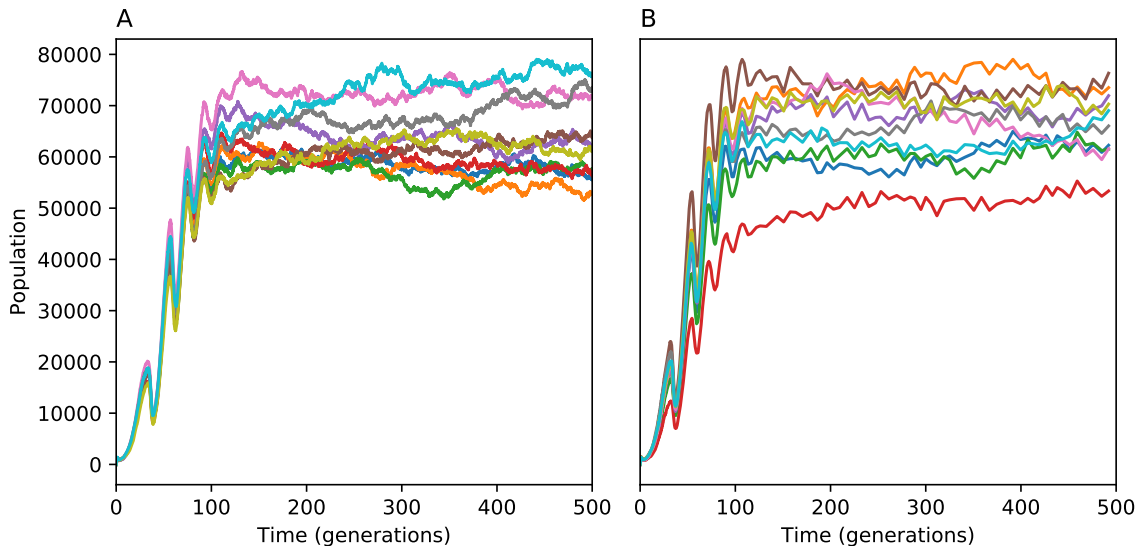


Figure 11: Comparison of individual spacer type trajectories using tau leaping and Gillespie simulations. (A) 10 spacer type trajectories vs time using Gillespie simulation methods. (B) 10 spacer type trajectories vs time using tau leaping simulation methods.

B.4 Parameter choices

Burst size for phage that target *S. thermophilus* is between 140-200 [70]. The rate of adsorption for phage is of the order of $10^{-8} \text{ min}^{-1} \text{ ml}$ [71]. Using a volume of $V = 50 \text{ ml}$, our total adsorption rate is $\alpha = 2 \times 10^{-10} \text{ min}^{-1}$ per bacteria and phage.

[72] measured the maximum growth rate of *S. thermophilus* in milk at 42C to be $2.4 \times 10^{-2} \text{ min}^{-1}$. This corresponds to gC_0 in our model.

The other parameters were picked in order to get a stable fixed point where phage and bacteria coexist, with population sizes relevant to experiments such as [1].

B.5 Simulation results

Our simulations were performed with a maximum of $m = 500$ spacer types that can be acquired by bacteria. This upper limit on the number of spacer types limits the total diversity of spacer types that can be observed and only impacts the spacer abundance distribution at large η . The qualitative simulation results, namely a continuous turnover of individual spacers and the presence of a non-trivial steady-state spacer abundance distribution, are insensitive to the choice of η provided not all m spacer types are acquired. This puts an upper bound on η of $\approx 10^{-4}$ in our simulation, but simulations with higher η can be performed with large values of m .

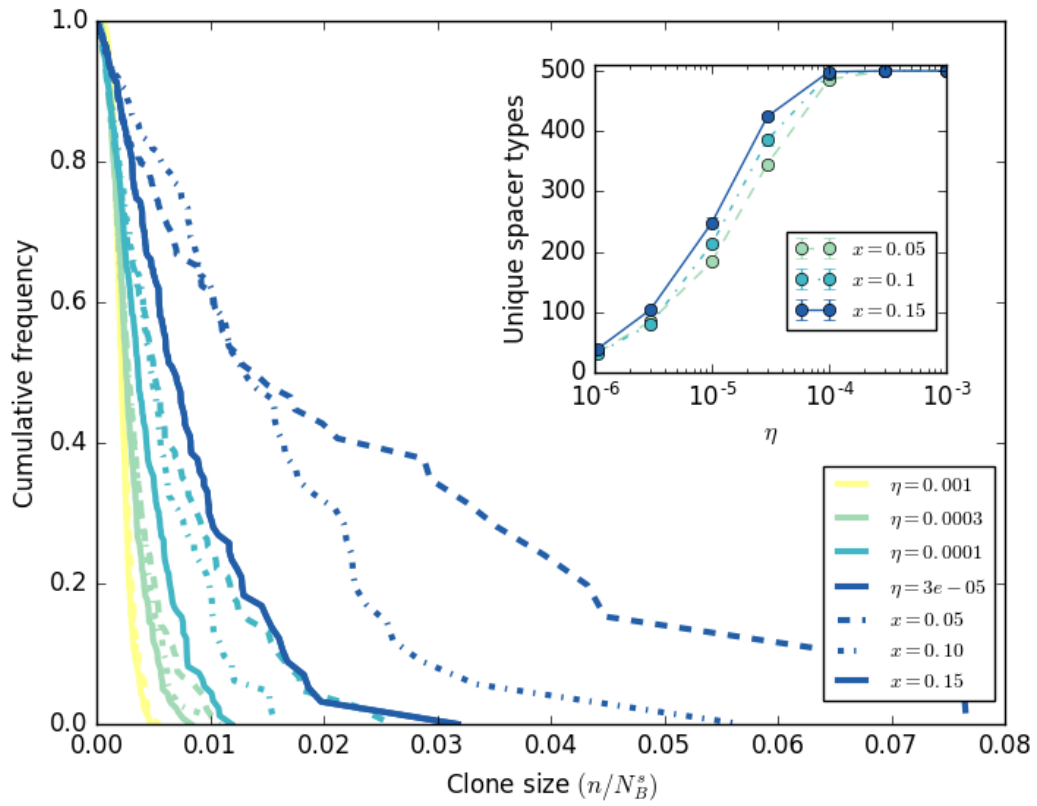


Figure 12: Distribution of spacer abundances along population contours (dash type) for different values of acquisition rate η (yellow to blue). Inset: number of unique spacer types acquired by bacteria at the end of the simulation increases with increasing η .

C Steady-state solutions

C.1 $e = 0$ model (no adaptive immunity)

Equations 3 to 5 describe the full model. If spacer effectiveness $e = 0$, the model reduces to three dimensions: bacteria n_B , phages n_V , and nutrients C . Equations 25 to 27 describe this simpler model.

$$\frac{dn_V}{dt} = -\alpha n_B n_V + \alpha B p_V n_B n_V - F n_V \quad (25)$$

$$\frac{dn_B}{dt} = g C n_B - \alpha p_V n_V n_B - F n_B \quad (26)$$

$$\frac{dC}{dt} = F C_0 - g C n_B - F C \quad (27)$$

Solving equations 25 to 27 at steady state gives the following fixed points.

C.1.1 Trivial fixed point

There is a trivial fixed point where bacteria and phages are both zero.

$$n_B^* = 0$$

$$n_V^* = 0$$

$$C^* = C_0$$

The eigenvalues of the Jacobian at this fixed point are $1 - f$, $-f$, and $-f$, where $f = F/(gC_0)$. This means that this fixed point is stable for $f > 1$. $f > 1$ is a reasonable stability condition: this is the case where the flow rate is too high for bacteria to persist.

C.1.2 Phages unable to persist

$$n_B^* = C_0(1 - f)$$

$$n_V^* = 0$$

$$C^* = C_0 f$$

$0 < f < 1$ is required for physical existence of this fixed point.

The eigenvalues of the Jacobian at this fixed point are $f - 1$, $-f$, and $-\frac{(f-1)p(Bp_V-1)+fp_V}{p_V}$, where $p = p_V \alpha / g$. The first two are negative under the requirement for existence. The third is negative for $Bp_V < \frac{gf}{(1-f)\alpha} + 1$. If this stability condition is satisfied, phages cannot persist in the population — they will be driven to extinction.

C.1.3 All populations finite and stable

If all variables are non-zero, the fixed point is

$$\frac{n_B^*}{C_0} = \frac{fp_V}{p(-1+Bp_V)}$$

$$\frac{n_V^*}{C_0} = \frac{(1-f)p(Bp_V-1)-fp_V}{p(p(Bp_V-1)+p_V)}$$

$$\frac{C^*}{C_0} = \frac{p(Bp_V-1)}{p(Bp_V-1)+p_V}$$

The condition for existence is

$$Bp_V > \frac{gf}{(1-f)\alpha} + 1$$

The eigenvalues are

$$\begin{aligned} & -f \\ & -\frac{\sqrt{f}\sqrt{4(f-1)p^2(Bp_V-1)^2+4fpp_V(Bp_V-1)+fp_V^2+fp_V}}{2p(Bp_V-1)} \\ & \frac{\sqrt{f}\sqrt{4(f-1)p^2(Bp_V-1)^2+4fpp_V(Bp_V-1)+fp_V^2}-fp_V}{2p(Bp_V-1)} \end{aligned}$$

The first is always negative. The second is negative for

$$\frac{4p^2(Bp_V-1)^2}{(2p(Bp_V-1)+p_V)^2} \leq f < 1$$

The third is negative for

$$\frac{4p^2(Bp_V-1)^2}{(2p(Bp_V-1)+p_V)^2} \leq f < \frac{p(Bp_V-1)}{p(Bp_V-1)+p_V} = \frac{C^*}{C_0}$$

The upper limit on f is the same as the existence condition (requiring all be solutions > 0).

C.2 Nonlinear bacterial growth rate

Instead of the growth rate for n_B being gC , we check what happens when the growth rate is a Hill function of the form $\frac{gkC}{C+k}$, where k is the nutrient concentration at which bacterial growth rate is at half maximum. If $k \gg C$, the linear approximation used in our results is valid and $\frac{gkC}{C+k} \approx gC$.

Solving for the non-trivial steady-state variables in the case when bacteria have no CRISPR spacers, we find:

$$n_B^* = \frac{F}{\alpha(Bp_V - 1)} \quad (28)$$

C^* and n_V^* now depend on k :

$$C^* = \frac{1}{2} \left(C_0 - k - \frac{gkn_B^*}{F} \right) + \frac{1}{2} \sqrt{\left(C_0 - k - \frac{gkn_B^*}{F} \right)^2 + 4C_0k} \quad (29)$$

$$n_V^* = \frac{gkC^*}{C^* + k} - F \quad (30)$$

This solution for C converges to the linear growth rate solution (section C.1.3) when k is large. Expanding the square root in C^* and keeping terms up to order $\frac{1}{k^3}$:

$$\frac{C^*}{C_0} \approx 1 - \frac{1}{p(B-1/p_V)} + \frac{1}{p^2(B-1/p_V)^2} \approx \frac{p(B-1/p_V)}{p(B-1/p_V)+1}$$

The stability condition for bacteria and phage coexistence now depends on k . k must be greater than the following parameter combination in order for phages to persist.

$$k > \frac{F(F + \alpha(C_0 - BC_0p_V))}{Fg + \alpha(F - C_0g)(Bp_V - 1)} = C_0 \frac{f(fg + \alpha(1 - Bp_V))}{fg + \alpha(1 - f)(1 - Bp_V)}$$

For $f = F/(gC_0) = 0.1$, $B = 170$, $p_V = 0.02$, $g = 2.4 \times 10^{-11}$, $C_0 = 10^9$, and $\alpha = 2 \times 10^{-10}$, k/C_0 must be greater than ≈ 0.11 . Figure 13 compares the full nonlinear growth solutions (equations 28 to 30) to the solutions for linear growth (equations C.1.3). Provided k is large enough that phages can persist, the picture is not qualitatively different, and in the low-nutrient limit ($k \gg C$), the two solutions are very nearly the same.

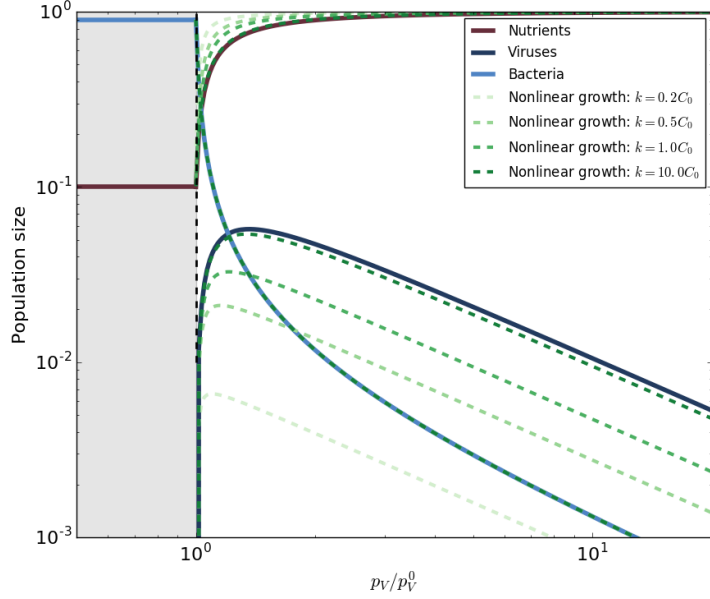


Figure 13: Solid lines: solutions to equations 25 to 27 with linear growth for n_B . Green dashed lines: solutions to equations 28 to 30 for different values of k .

C.3 $e \neq 0$ model (adaptive immunity)

If $e > 0$, then the system is fully four-dimensional and all four variables are coupled.

C.3.1 Trivial fixed points

The two partially trivial fixed points are the same as in the case when $e = 0$, since if $n_V = 0$, then $\nu = 0$ at steady state. The stability and existence conditions are also the same; effectively ν becomes uncoupled and the system is reduced to three dimensions if $n_V = 0$.

C.3.2 Non-trivial fixed point

For convenience we define rescaled population sizes $x = n_B/C_0$, $y = n_V/C_0$, and $z = C/C_0$. Solving in the case where all dynamical variables are non-trivial, we get

$$z^* = \frac{p(Bp_V(ev^* - 1) + 1)}{p(Bp_V(ev^* - 1) + 1) - p_V} \quad (31)$$

$$x^* = \frac{fp_V}{p} \frac{1}{Bp_V(1 - ev^*) - 1} \quad (32)$$

$$y^* = \frac{(f - 1)p(Bp_V(ev^* - 1) + 1) - fp_V}{p(ev^* - 1)(p(Bp_V(ev^* - 1) + 1) - p_V)} \quad (33)$$

And an implicit cubic equation for ν , where $R = r/(gC_0)$:

$$0 = (1 - \nu) [-p_V \nu e - \eta(1 - p_V)] [(1 - f)p(p_V B(1 - e\nu) - 1) - fp_V] + R\nu p_V(1 - e\nu)(Bpp_V(1 - e\nu) - p + p_V) \quad (34)$$

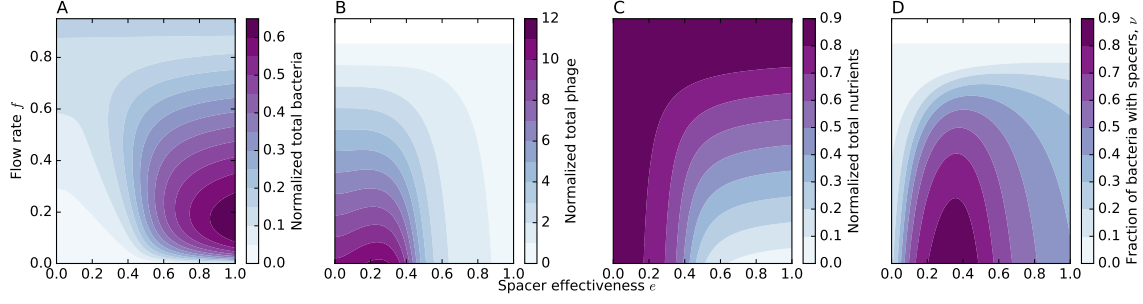


Figure 14: x , y , z , and ν (A-D respectively) vs. f and e with $R = 0.04$, $\eta = 0.0001$, $B = 170$, $p_V = 0.01$, $\alpha = 2 \times 10^{-10}$, and $gC_0 = 0.024$.

This cubic equation is analytically solvable, but the full solutions in terms of all parameters are cumbersome.

Only one of the three solutions of equation 34 is physical in the parameter range we use (real-valued and properly bounded):

$$\nu^* = -\frac{(1 + i\sqrt{3}) \sqrt[3]{\sqrt{(-27a^2d + 9abc - 2b^3)^2 + 4(3ac - b^2)^3} - 27a^2d + 9abc - 2b^3}}{6\sqrt[3]{2}a} + \frac{(1 - i\sqrt{3})(3ac - b^2)}{3 \cdot 2^{2/3}a \sqrt[3]{\sqrt{(-27a^2d + 9abc - 2b^3)^2 + 4(3ac - b^2)^3} - 27a^2d + 9abc - 2b^3}} - \frac{b}{3a} \quad (35)$$

where the coefficients are

$$a = Be^2 f p p_V^2 (f + R - 1) \quad (36)$$

$$b = -e f p_V (p(f(B(p_V(e + \eta + 1) - \eta) - 1) + B(\eta - p_V(e + \eta - 2R + 1)) - R + 1) + p_V(f + R)) \quad (37)$$

$$c = f p [B p_V^2 (e(f - 1)(\eta + 1) + (f - 1)\eta + R) - (e - 1)(f - 1)p_V(B\eta + 1) - (2B + 2)(f - 1)\eta p_V + (f - 1)\eta - p_V(f + R - 1)] + f p_V (e f p_V - f \eta + p_V(f \eta + R)) \quad (38)$$

$$d = -f \eta (p_V - 1)((f - 1)p(B p_V - 1) + f p_V) \quad (39)$$

Total bacteria, phage, nutrients, and the fraction of bacteria with spacers are plotted for a range of parameters in Figure 14 and Figure 16.

This fixed point is stable for a wide range of parameters, which we explored numerically. Figure 15 shows the number of negative eigenvalues vs. parameters; where all four eigenvalues have a negative real part, this fixed point is stable.

C.3.3 Large α limit

For large α ($\alpha \gg \alpha_0$, where $\alpha_0 = \frac{gf}{(1-f)(B p_V - 1)}$), we can find an approximate value of e , e^* , at which ν and n_V peak (equation 40). This solution is plotted as a yellow dashed line in Figure 16.

$$e^* = \frac{1}{B p_V} + \frac{R(1 - B p_V)}{B p_V (f - 1)(1 - B(\eta + p_V) + B \eta p_V)} \quad (40)$$

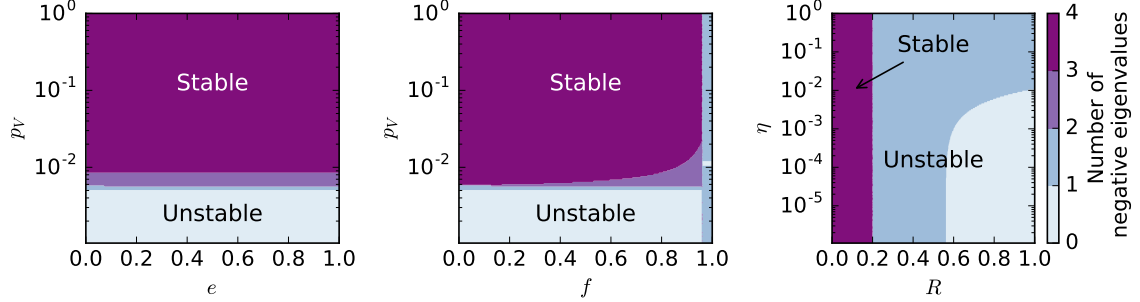


Figure 15: The number of eigenvalues with a negative real part for various parameter combinations (p_V and e , p_V and f , and R and η). The unstable regions in the first two plots reflect parameter combinations for which phages cannot persist. In the third plot, Equation 35 becomes unstable for large R , but one of the other roots takes its place as a stable and physical solution in this regime (confirmed numerically).

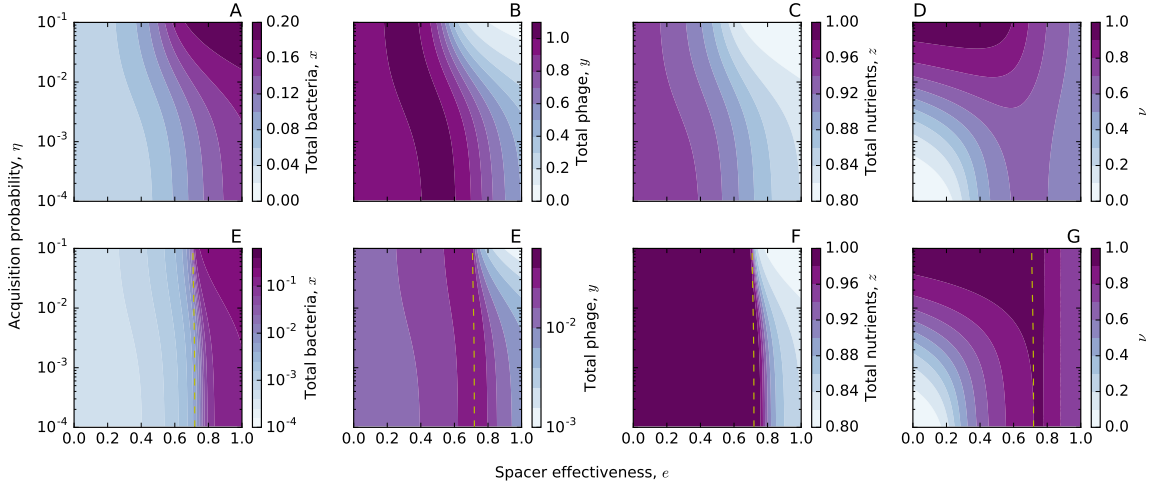


Figure 16: x , y , z , and ν vs. η and e for $\alpha \gtrsim \frac{gf}{(1-f)(Bp_V-1)}$ (top row) and $\alpha \gg \frac{gf}{(1-f)(Bp_V-1)}$ (bottom row). The yellow dashed line is the approximate value of e at which both ν (G) and y (F) are maximized (equation 40) which agrees well with the full solution for large α .

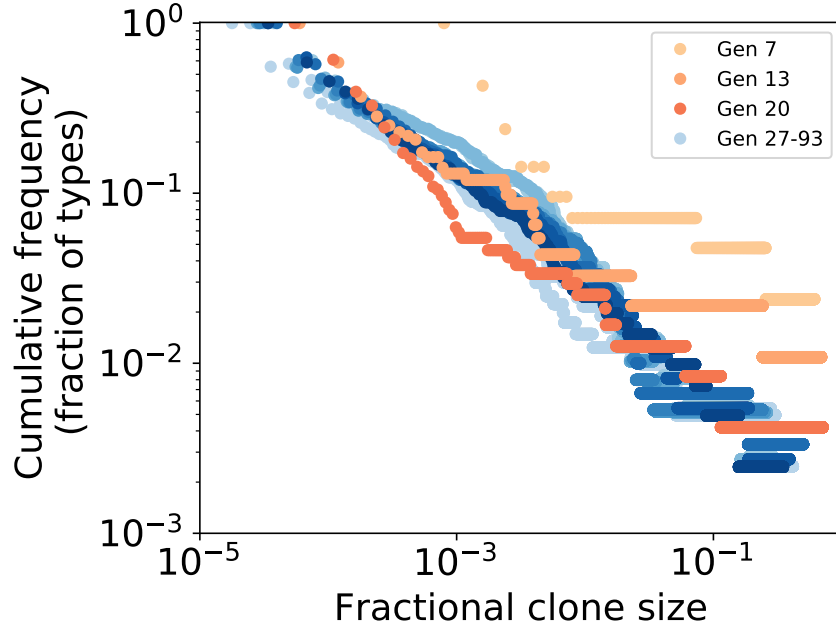


Figure 17: Cumulative frequency of spacer types (clones) as a function of normalized clone size. Darker blue indicates earlier times.

D Spacer dynamics

In our analysis of data from [1], we found that spacer abundance distributions were stable in time after three days and were broad, spanning four orders of magnitude. This distribution $\rho(v)$ is created by summing all spacer types of a particular abundance: $\rho(v) = \sum_i \delta(n_B^i - v)$. The normalized cumulative distribution, $\sum_v^\infty \rho(v) / \sum_0^\infty \rho(v)$, is plotted in (Figure 17). The corresponding rank-abundance distribution is plotted in Figure 3C in the main text.

Individual spacer types experience continual turnover, both in our simulations and in experimental data from [1]. In the experimental data, both high-abundance and low-abundance spacers can change in abundance by an order of magnitude or more between time points, while in our simulations we find that the large abundance spacers are approximately stable once the system has reached a population-level steady state (Figure 18).

The observed turnover in large spacer types in the experimental data may reflect additional stochasticity not accounted for in our model, changes in fitness for individual spacer types over time, or the fact that the sequenced spacers are strongly undersampled. There are $\approx 10^8$ to 10^9 bacteria at the end of each day in the experiment, and there are $\approx 3 \times 10^4$ spacers recovered from sequencing each day. The data is undersampled by a factor of $\approx 10^4$, and apparent turnover may result from this.

Figure 19 compares the original simulation data with data undersampled by a factor of 10^2 , 10^3 , or 10^4 . The mean abundance over time for a particular type appears mostly unaffected by the undersampling, but there is indeed more variability when the degree of undersampling is higher. At an undersampling factor of 10^4 , spacer counts are in the ones and tens, much lower than than counts of $\approx 10^3$ or 10^4 in the experimental data. Variability in the experimental data is over more orders of magnitude between time points than in the undersampled simulated data.

This undersampling of simulated data only considered that fewer organisms are sequenced than are present in the population and does not take into account that the experiment was performed with

100:1 serial dilutions and so each time point was seeded with a random subsample from the previous time point.

E Regulation of CRISPR-Cas

E.1 Extent of bistability

We add regulation of CRISPR-Cas to our model by making spacer effectiveness e a function of bacterial cell density, assuming Cas expression to also be a sigmoidal function of cell density. Many bacterial behaviours controlled by quorum sensing are threshold-dependent: cells must switch between discrete states such as motile and non-motile, biofilm and free-living, virulent and non-virulent. In many quorum sensing systems, production of the autoinducer molecule is under positive feedback and increases nonlinearly with increasing cell density, and so many of the resulting changes in gene expression are switch-like [73]. For this reason we assume that spacer effectiveness depends strongly on cell density.

However, we observe bistability for a wide range of parameters and note that spacer effectiveness does not necessarily need to be a sharp function of x , where $x = n_B/C_0$. Figure 20 illustrates the additional dependence of e on x — wherever $e(x)$ intersects the original solution, there is a fixed point. Figure 20B shows that even a linear $e(x)$ can intersect the original solution in three places for certain parameters, in this case certain values of f . Any curve that intersects one of the solid lines in three places will result in bistability.

Changing the precise location of the transition from low to high spacer effectiveness does not change the existence of bistability, but it does cause an interesting bifurcation. Figures 21 and 22 show in two and three dimensions what happens to the fixed points as the transition point is scanned from low to high. For a transition point at low cell density, the unstable fixed points are adjacent to the low expression stable fixed points at one end and the high expression stable fixed points at the other end, making hysteresis possible. However, as the transition point increases to higher cell density, the two ends meet and form a closed loop with just the high expression state. In this situation, bistability still exists, but the system can never jump from the low expression state to the high expression state without being placed there since there is one continuous low expression stable state across the entire range of f .

E.2 Bistability across system variables

Bistability affects all four dynamical variables in our model. Figure 23 shows each variable at steady state vs. flow rate f in a regime with bistability.

E.3 Adding regulation to acquisition, loss, and growth rate

We model CRISPR-Cas regulation by making spacer effectiveness density-dependent, but it is reasonable that up-regulation of CRISPR-Cas would affect other system parameters as well. In particular, spacer acquisition rates would likely increase since acquisition relies on the Cas protein machinery as does interference [40]. Additionally, spacer loss is thought to happen by homologous recombination and to occur in tandem with acquisition [57, 34].

We added a sharp sigmoidal density dependence to both spacer acquisition probability and spacer loss rate. Figure 24 shows the resulting steady-state bacterial population size as a function of spacer effectiveness. The result is still monotonically increasing, which means that a monotonic function for spacer effectiveness as a function of x can still only intersect in at most three places, qualitatively giving the same bistability result.

Measurements of the fitness cost of CRISPR in *Streptococcus thermophilus* identified Cas protein expression as having a fitness cost [5], making it reasonable that bacteria would down-regulate Cas expression in times when CRISPR is not needed. [5] measured a selective advantage of 0.11 for *S. thermophilus* with a *cas9* or *csn2* gene knockout in direct competition with wild type but did not

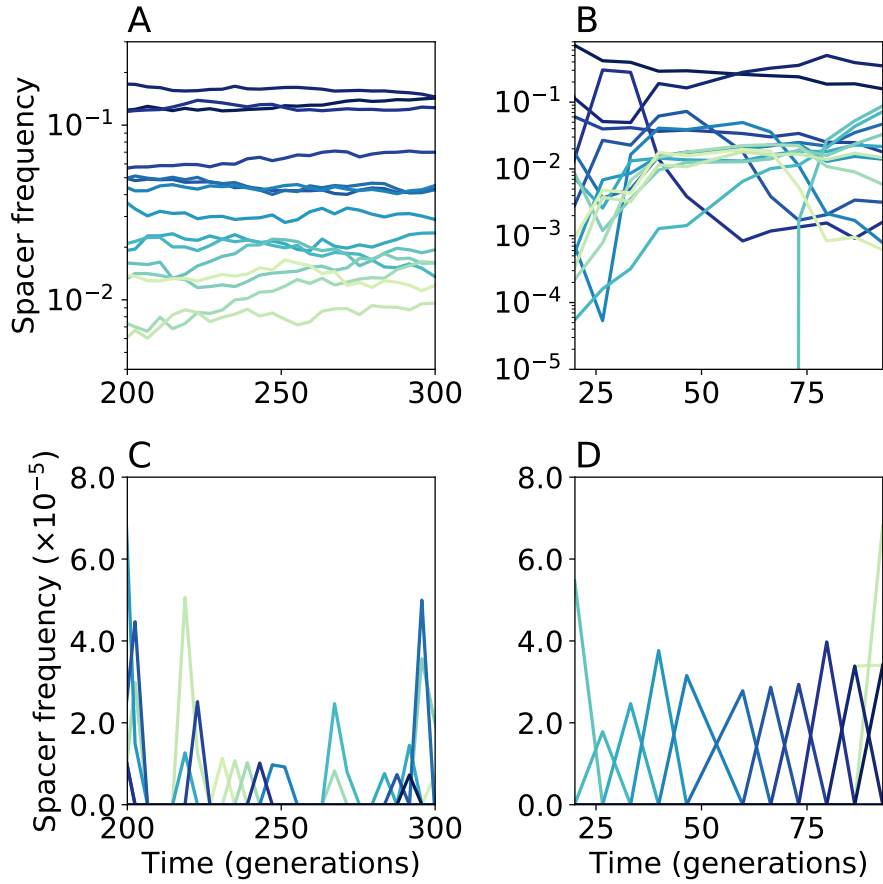


Figure 18: Spacer type trajectories vs. time for experimental data from [1] (B and D) and for data from our simulations (A and D). Colours indicate different spacer types. (A and B) show the largest 15 spacer types vs. time and (C and D) show the lowest 15 unique spacer type trajectories vs. time. Both large and small abundance spacers experience turnover in the experimental data, while in simulations the large abundance spacers are approximately stable once the system has reached population-level steady state.

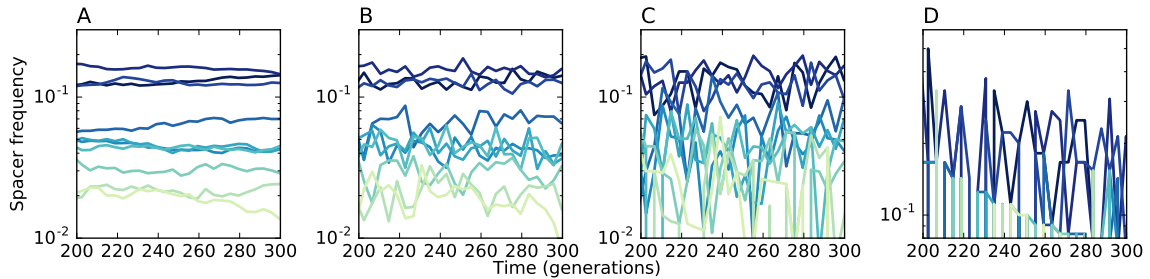


Figure 19: A comparison of the top 10 spacer types from the original simulation (A) with a randomly sampled subset of the simulated data (B, C, D). Spacers are sampled without replacement at every 50th simulation time point. Data is undersampled by a factor of 10^2 (B), 10^3 (C) and 10^4 (D).

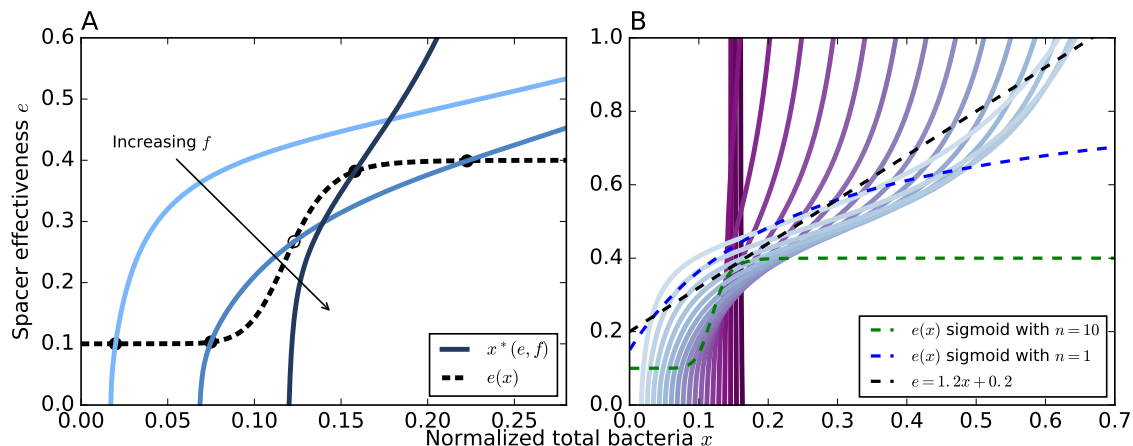


Figure 20: (A) The original dependence of bacterial population size at steady-state on spacer effectiveness e and normalized flow rate f is plotted for three values of f (solid blue lines). We model upregulation from quorum sensing by introducing a density-spacer effectiveness (dashed black line), $e(x) = e_{min} + (e_{max} - e_{min}) \left(\frac{x^n}{x^n + x_0^n} \right)$, so that spacer effectiveness is no longer a constant parameter. Any intersection of the dashed line with a solid line is a fixed point; fixed points are indicated with solid circles (stable) and open circles (unstable). (B) Spacer effectiveness e vs. bacterial population size at steady-state for different values of f (solid lines). Line colour darkens as f increases. Three different choices of $e(x)$ are plotted (dashed lines), all of which intersect some of the solid curves in three places, indicating bistability.

observe a difference in maximum growth rate. This definition of selective advantage corresponds to the difference in average exponential growth rate per hour for each strain. We incorporated a Cas-expression-dependent decrease in bacterial growth rate in our model and investigated its effect on bistability. We model Cas expression as a theta function (discrete ‘off’ and ‘on’ states) with the switch occurring at $x_C = 0.06$ (arbitrarily chosen).

$$g(x) = \begin{cases} g_1 & x \leq x_C \\ g_0 & x > x_C \end{cases} \quad (41)$$

The growth rate gC_0 depends on the Cas expression state with g_1C_0 being the growth rate per minute without Cas expression and g_0C_0 being the growth rate with Cas expression, where $g_0 < g_1$. A selective advantage of 0.11 gives $g_0 = g_1 - 0.11/(60C_0)$.

Figures 25 and 26 show the resulting change in steady-state bacterial population size as a function of spacer effectiveness for two different growth rate dependences on expression. For even a 50 percent reduction in growth rate at high Cas expression, the resulting curves are not qualitatively altered, and as before, a monotonic curve for $e(x)$ can intersect in at most three places to give bistability.

E.4 Experimentally measuring regulation

While we chose parameters that are reasonable for *S. thermophilus*, it is unlikely that our quantitative results match experimental conditions for different organisms. Our prediction is that in an appropriate parameter range, an experiment measuring bacterial population density as a function of flow rate may exhibit hysteresis as the flow rate is first increased and then decreased, allowing the bacteria-phage population to reach steady state after each change in flow rate. It is easy to imagine however that the transition determining high or low Cas expression may not automatically align with the cell densities

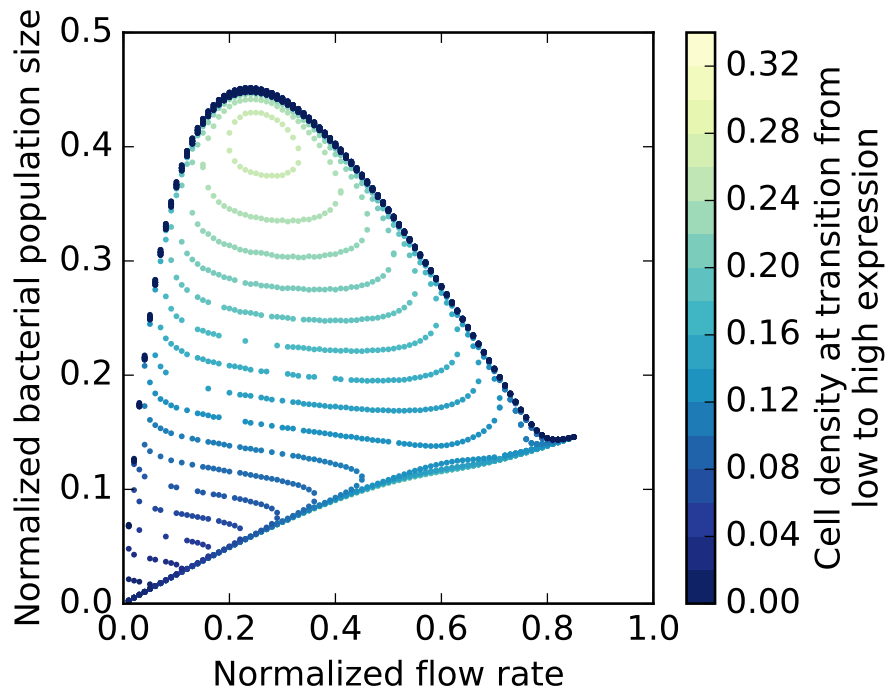


Figure 21: Fixed points (bacterial population size) as a function of flow rate f for different values of the transition point between low and high expression. As the transition point increases (lighter colours), the bistability changes from an ‘S’ shape to a circle and a line. This bifurcation happens at a transition point of approximately $x = 0.15$.

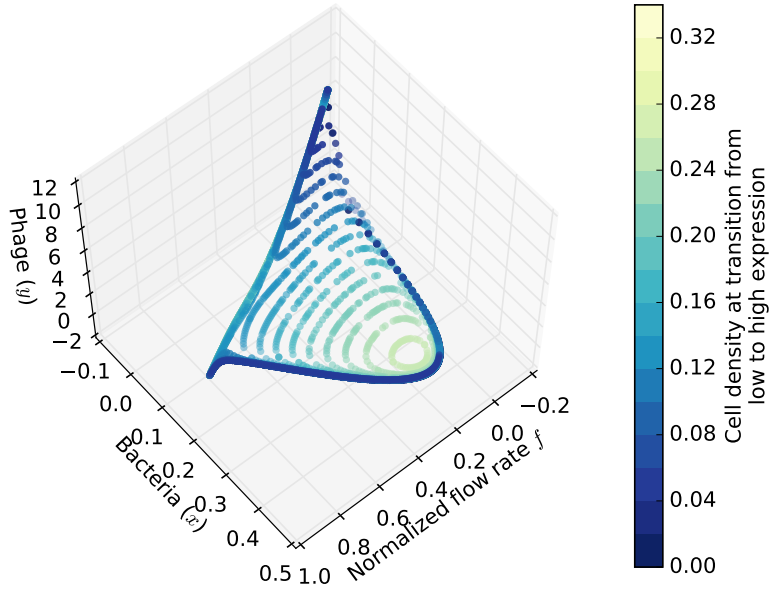


Figure 22: Fixed points (bacterial population size and phage population size) as a function of flow rate f for different values of the transition point between low and high expression.

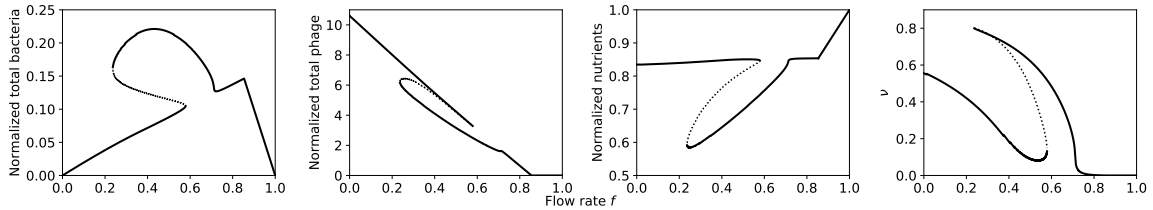


Figure 23: Bacteria x , phages y , nutrients z , and the fraction of bacteria with spacers ν as a function of f in a parameter regime showing bistability. The solid black lines indicates a stable fixed point and the dashed black line indicates an unstable fixed point.

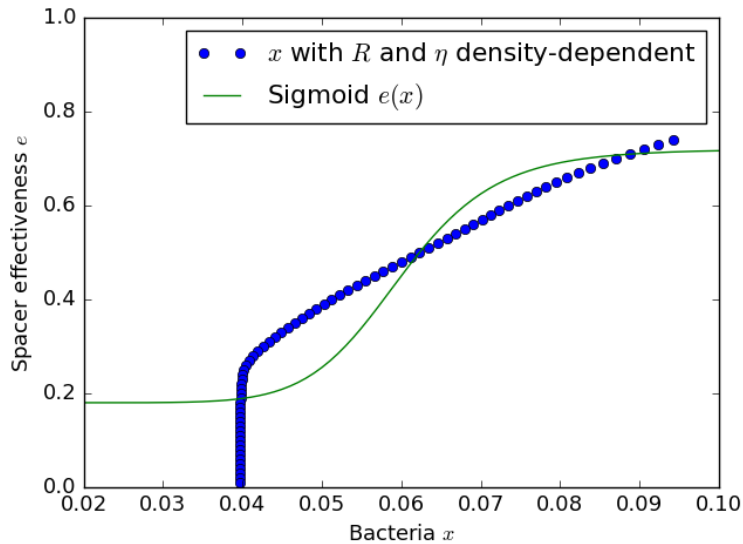


Figure 24: The dependence of bacterial population size x at steady-state on spacer effectiveness e when r and η are both sharp functions of density (blue dots). A monotonic function for spacer effectiveness as a function of x (green solid line) can still only intersect in at most three places, qualitatively giving the same bistability result.

in the chemostat. The first experimental step is to measure the true Cas expression as a function of cell density for *Pseudomonas*, as done in [28]. In their experiment, *cas3* expression increased by a factor of about 10 for a 10-fold increase in cell density (from $\approx 8 \times 10^7$ to $\approx 8 \times 10^8$ CFU/mL).

Next, the concentration of nutrients in the inflow medium C_0 can be used to tune the cell density to one at which CRISPR would naturally be highly expressed at a high flow rate. Then the flow rate F can independently tune the position along the bifurcation diagram in Figure 4. In this way an experimental population of *Pseudomonas* can be tweaked to qualitatively align with our model.

Figure 27 shows the steady-state bacterial concentration vs. spacer effectiveness in our model as C_0 and F are varied. Provided the true Cas expression is a sharp enough function of density and that the low expression state is below the plateau in effectiveness in Figure 27, it will be possible to choose C_0 and F such that the system is bistable. The position of the plateau in effectiveness at which the bacterial density changes sharply is controlled by Bp_V : as Bp_V increases, the plateau moves to higher effectiveness.

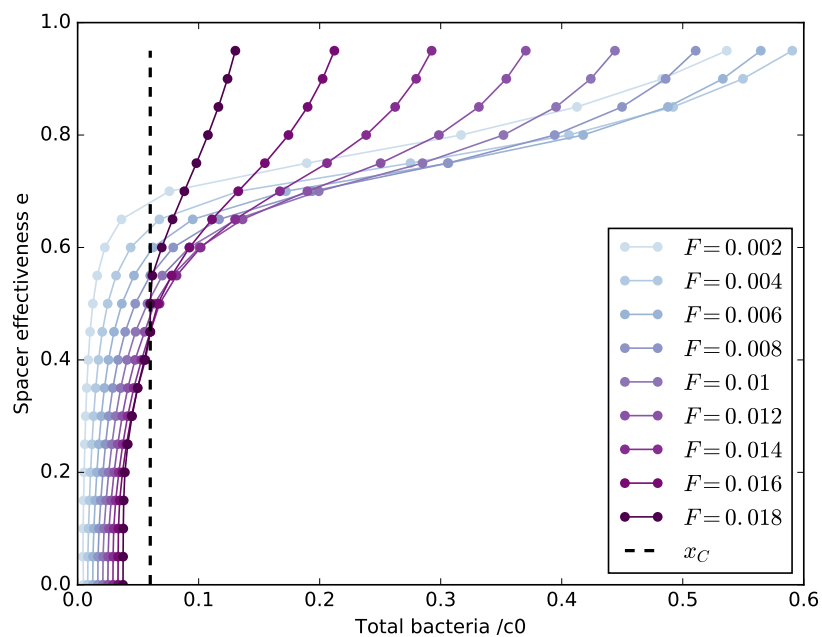


Figure 25: The dependence of bacterial population size x at steady-state on spacer effectiveness e when g is a sharp function of cell density x . The value of x at which regulation is turned on or off is indicated by the black dashed line. Lines are plotted for F instead of $f = F/(gC_0)$ because f depends on g . Plotted is bacterial population size at steady state where the growth disadvantage for Cas expression is $g_0 = g_1 - 0.11/(60C_0)$, calculated from the measured selection coefficient in [5].

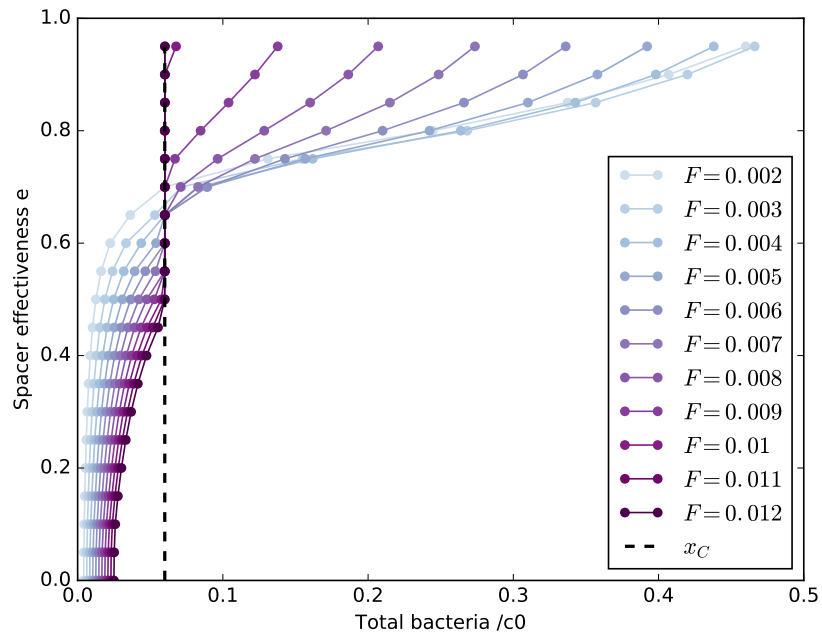


Figure 26: The dependence of bacterial population size x at steady-state on spacer effectiveness e when g is a sharp function of cell density x . The value of x at which regulation is turned on or off is indicated by the black dashed line. Plotted is bacterial population size at steady state where the growth disadvantage for Cas expression is $g_0 = 0.5g_1$.

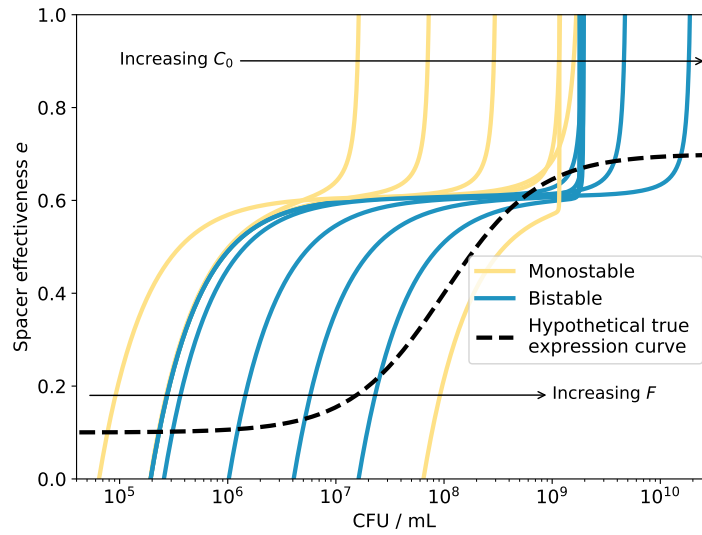


Figure 27: The dependence of bacterial population size x at steady-state on spacer effectiveness e in the model for different values of F and C_0 (solid lines). For a given measured dependence of *cas* expression on cell density (black dashed line, for example), F and C_0 can tune whether the system is monostable or bistable by changing the number of intersections between the two curves.